Article:
Gou, Q., Chen, S., Du, Y. et al. (2026) A new model for quantitative analysis of kinematic properties of faults: Examples from the Jiyang Depression, NE China. Journal of Asian Earth Sciences, 295. 106829. ISSN: 1367-9120

https://doi.org/10.1016/j.jseaes.2025.106829

A new model for quantitative analysis of kinematic properties of faults: Examples from the Jiyang Depression, NE China

Qiwei Gou [a, b, c], Shuping Chen [a, b], Yifan Du [a, b], Adam D. McArthur [c], Nigel P. Mountney [c], Haowei Yuan [d, e], Xi Li [a, b], Huaibo Zhao [a, b]

a State Key Laboratory of Petroleum Resources and Engineering, China University of Petroleum (Beijing), Beijing 102249, China

b College of Geosciences, China University of Petroleum (Beijing), Beijing 102249, China

c School of Earth and Environment, University of Leeds, Leeds LS2 9JT, UK

d National Key Laboratory of High-Efficiency Flexible Coal Power Generation and Carbon Capture Utilization and Storage, Beijing 102209, China

e China Huaneng Clean Energy Research Institute, Beijing 102209, China

*Corresponding author:

E-mail address: csp21c@163.com (Shuping Chen).

Permanent Address: State Key Laboratory of Petroleum Resources and Engineering, China University of Petroleum (Beijing), Beijing 102249, China.

Abstract: Calculating the strike-slip component of fault displacement is challenging,

making quantitative determination of the kinematic properties of a fault zone difficult. This study introduces a novel fault zone model to offer improved opportunities to reconstruct the history of fault evolution. We provide a new quantitative calculation method of fault geometry that can identify piercing points where branch faults are offset by a master fault. This method is based on the geometric relationships between the attitude of a master fault and its branch faults. From these observations, it is possible to quantitatively calculate the displacement components and kinematic properties of a fault zone. Additionally, the existing stereographic projection method is adapted by considering the attitude of fault planes to provide an alternative approach to solve the problem of fault kinematics. This method can be used to derive the pitch angle of a fault with the new model by analyzing the intersection attitudes of a master fault and its branch faults through intersecting planes. Applied to 3D seismic data with well control from the Jiyang Depression, results show higher strike-slip intensity near principal displacement zones adjacent to the Tan-Lu and Lan-Liao fault zones, whereas extensional deformation dominates the central sector. Moreover, both methods yield consistent results in reconstructing the structural history of fault zones. This demonstrates the practical application of the new model and demonstrates that methods employed for the model can be used in the kinematic analysis of fault zones more generally, which has previously been challenging in subsurface studies.

Keywords: structural analysis, stereographic projection, strike-slip fault, true pitch

angle, fault geometry

1. Introduction

The nature and direction of the principal stress of a fault is commonly determined in two ways: (i) via the attitude of slickensides and steps preserved on exposed fault planes at outcrop to reveal the orientation of slip; (ii) via examination of the geometric features of faults and the thickness variations of stratal units preserved on either side of a fault to identify stress properties, such as flower structures indicating strike-slip property and thickness differences between the two walls of growth faults (Biddle and Christie-Blick, 1985; Woodcock and Rickards, 2003; Le Guerroué and Cobbold, 2006; Zhang et al., 2017; Fletcher et al., 2020; Jia et al., 2022). Since the 1970s, investigations of the history of fault activity have become increasingly detailed, enabling to more accurate reconstructions of fault evolution (Molnar and Tapponnier, 1977; Fu et al., 2015; Dimmen et al., 2017; Zhou et al., 2019; Ma et al., 2023). To quantitatively study the evolutionary history of faults, numerous methods have been proposed: (i) determination of the strike-slip and dip displacement components of faults to identify the history of fault motion (Mansinha and Smylie, 1971; Marrett et al., 1990; Peacock, 1991;Yu et al., 2008; Hughes, 2012; Lu et al., 2018a; Walker et al., 2021; Yu et al., 2021); (ii) examination of the interaction and displacement transfer between active intersecting strike-slip (or transform) and extensional fault systems by establishing a vertical intersection model (Garfunkel and Ron et al., 1985; Mouslopoulou et al., 2007); (iii) analysis of 3D and 4D geological relationships via sandbox analogue modelling or 3D numerical modelling (Dooley et al., 1999; Gogonenkov and Timurziev, 2012; Lindsay

et al., 2012; Stefanov and Bakeev, 2014; Fedorik et al., 2019), and (iv) application of the fracture development index (Fossen and Rotevatn, 2016; Jolly et al., 2016; Sançar et al., 2020). These works have not only advanced the development of quantitative analytical methods in structural geology, but have also helped to demonstrate the influence of faulting on sedimentation in considerable detail (Morley, 2007; Dooley and Schreurs, 2012; Gou et al., 2020; Liu et al., 2020; Hu et al., 2022).

Although the aforementioned methods for the calculation of fault activity displacement, for characterizing fault-slip direction, and for the quantification of fault kinematic properties have been established for many years, several persistent challenges remain. Notably, to calculate the strike-slip displacement component of a fault, it is necessary to identify and locate piercing points consisting of paired linear features occurring on either side of a fault plane. Distinctive features, such as river channels (or channel-fills), fold axes, or matched igneous rocks are commonly used as reference points (Benesh et al., 2014; Waldron et al., 2015; Ma et al., 2018). However, it is often challenging to identify such features in faulted geological settings, particularly in the subsurface where seismic reflection data are the principal data available. Therefore, it is important to address the following two challenges: (i) how to improve existing methods employed to locate fault piercing points and thereby to make models more accurate and universally applicable; and (ii) how to develop novel, simpler methods that may be applied more widely? Addressing these two research questions provides opportunities

to quantitatively and more accurately determine fault kinematic properties.

The aim of this study is to develop a novel model to investigate the properties of subsurface fault kinematics within sedimentary basins. This model considers different combinations of fault zone geometries, specifically describing two different styles of branch fault interaction with a master fault. Firstly, where a branch fault intersects a master fault tip. Secondly, where a branch fault intersects a master fault in its lateral part. Specific research objectives are as follows: (i) to establish a novel fault zone model for which piercing points can be more broadly identified and located than is possible when relying only on single distinctive geological bodies as piercing points; (ii) to develop a mathematical method to identify the kinematic properties of a fault zone using a quantitative calculation method, based on geometric relationships of the fault zone that combines the recognition of piercing points and the geometric features of fault planes in a fault zone model; (iii) to identify the kinematic property of a fault zone from a geological perspective by developing an adapted application of the stereographic projection method; (iv) to test the new model and methods in different fault zones using 3D seismic data and well data, where branch faults intersect a master fault at its tip and elsewhere along the master fault. This new model permits a more accurate reconstruction of fault zone evolution across a range of fault combinations.

2. Geologic setting

The Jiyang Depression (JYD) is situated in the southeastern region of the Bohai Bay Basin (BBB) in eastern China. The Bohai Bay Basin is a continental rift basin, which has undergone two stages of tectonic evolution: (i) a rifting stage during the Paleogene (65-24.6 Ma); (ii) a post-rifting stage during the Neogene-Quaternary (24.6 Ma-present) (Teng et al., 2019; Li et al., 2024).

The JYD is flanked by the Tan-Lu fault zone to the east and the Lan-Liao fault zone to the west. Its southern boundary is defined by the Luxi Uplift, and it is separated from the BBB by the Chengning Uplift to the north (Fig. 1). The depression formed during Mesozoic and Cenozoic on the Archean and Paleozoic basement of the North China platform, and serves as a typical example of a series of linked continental fault-bounded lacustrine-dominated sub-basins in China, characterized by a half-graben with northern faults and southern slopes (Zhang et al., 2014; Zuo et al., 2015; Zhang et al., 2017; Song, 2018; Zhou et al., 2019; Li et al., 2021; Yuan et al., 2022). The JYD is comprised of four sub-depressions; the Dongying, Zhuanghua, Chezhen and Huimin sags, which are separated by the Chenjiazhuang, Yihezhuang, Linfanjia uplifts (Fig. 1c).

The tectonic pattern of JYD results from the dual effects of both strike-slip and extension (Liu et al., 2018; Song, 2018). During the early Paleogene (E_1k_3 - E_2s_4), the depression experienced strong N-S extension, leading to the formation of numerous

normal faults (Yuan et al., 2022; Hu et al., 2022). Subsequently, in the late Paleogene (E_2s_3 - E_3d_1), right-lateral strike-slip dominated along the Tan-Lu fault zone, reactivating pre-existing faults (Yuan et al., 2022; Li et al., 2024). This shift coincided with increased Pacific Plate subduction rate, transitioning the basin from extension to differential compression (Liang et al., 2016). The E_2s_3 member (~42.0–38.0 Ma±) recorded peak strike-slip activity related to the shift in the direction and rate of the Pacific Plate subduction from NW to NWW, while the E_3s_2 member (~38–36 Ma) was tectonically quiescent (Cheng et al., 2018; Hu et al., 2019). Cumulative multi-stage processes generated extensive fault zones and unconformities (Zhang et al., 2014; Zhao et al., 2014; Liang et al., 2016; Yu et al., 2020; Li et al., 2021).

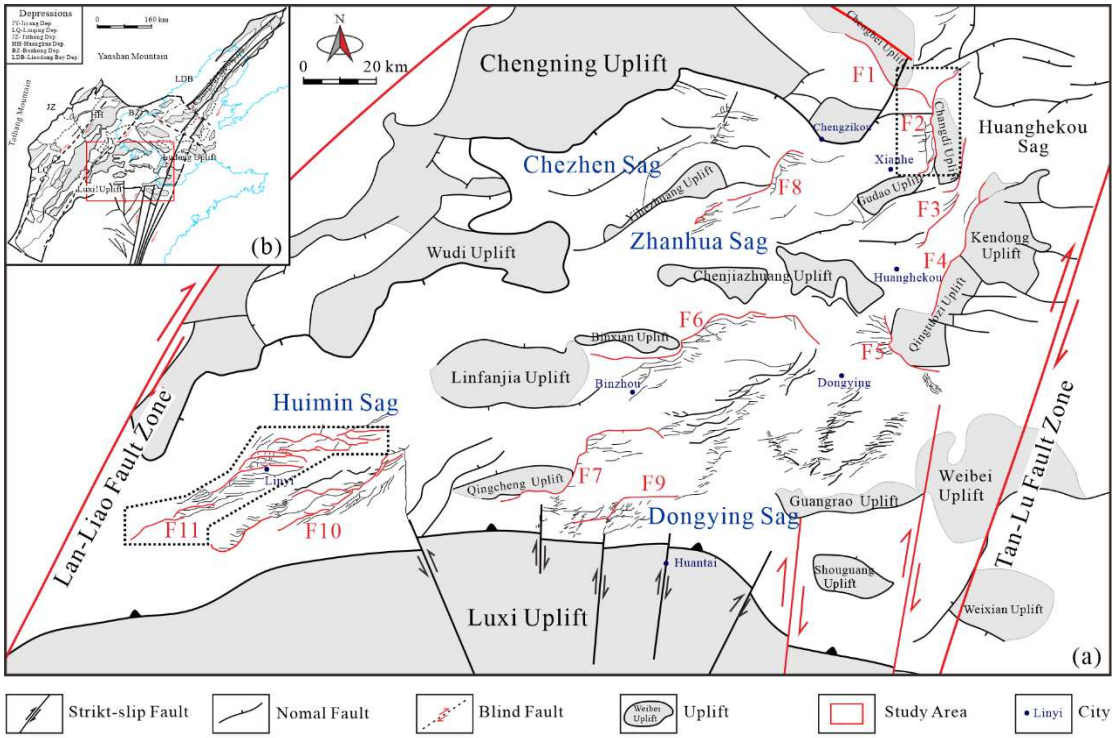

Fig. 1. Outline fault map of Jiyang Depression.

(a) Location of the Tan-Lu fault zone, Lan-Liao fault zone and the Jiyang Depression in the Bohai

Bay Basin. (b) Simple structural map of the Jiyang Depression during the Cenozoic, showing the major faults, uplifts and sags.

Following a discontinuity in deposition, an unconformity developed separating Mesozoic strata from the overlying Cenozoic sedimentary succession in JYD, which itself can be divided into six lithostratigraphic units: the Paleogene Kongdian (E_1k_3 - E_2k_1), Shahejie (E_2s_4 - E_3s_1) and Dongying (E_3d_1) formations, as well as the Neogene Guantao (Ng), Minghuazhen (Nm) formations and the Quaternary Pingyuan (Qp) Formation (Fig. 2). Syn-rift sequences (E_1k_3 - E_3d_1) exhibit progressive tectonic control. The interval bounded by reflectors T_6 (base of $E_2s_3^L$) and T_2 (base of E_3s_1) encompasses the E_2s_3 and E_3s_2 members. The E_2s_3 member comprises two distinct sub-members: a lower sub-member characterized by fan delta deposits and an upper sub-member dominated by turbidite deposits. Concurrently, the E_3s_2 member exhibits fan delta sedimentation. Collectively, these units record lacustrine-deltaic sedimentation during the late Eocene-early Oligocene (Liang et al., 2016; Chen et al., 2017; Xu et al., 2019; Zhu et al., 2021).

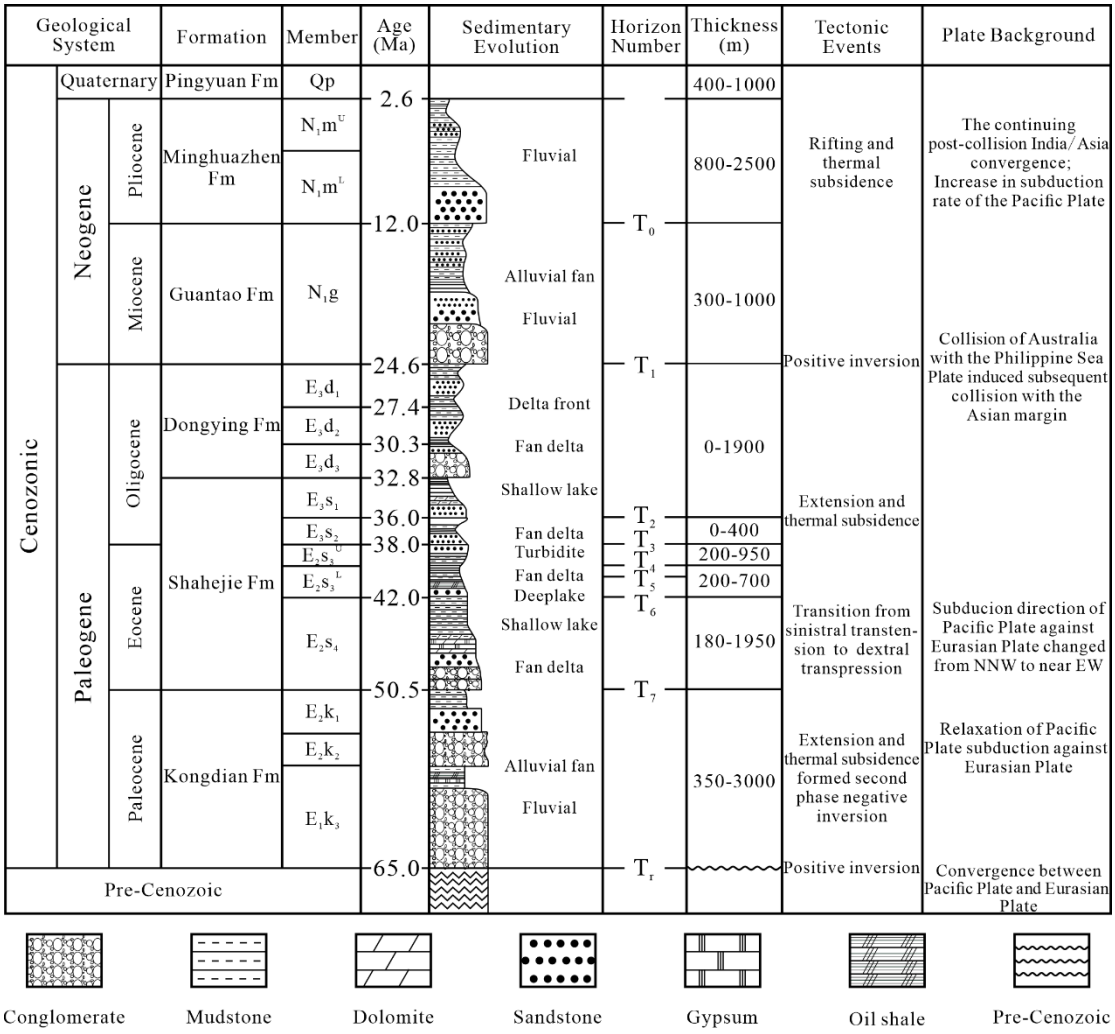

Fig. 2. Evolution process and generalized stratigraphy of the Dongying sag (modified from Su et al., 2009; Teng et al., 2019; Yuan et al., 2022). Fm = Formation.

3. Models and methods

Fault zones with diverse structural styles commonly develop in the same basin, notably in response to complex tectonic geological activities under varying stress regimes (Zoback et al., 1993; Ferrill et al., 2021). This is especially true in areas subject to two or more overlapping regional stresses, where the resultant stress combinations can vary, giving rise to features such as en echelon faults, broom-shaped faults (and variants thereof), and domino faults, as well as flower structures (Fu et al, 2015; Hu et al., 2019).

The slip line of a fault plane can accurately represent the kinematic properties of both the hanging wall and footwall of a fault. Projecting the slip line onto the horizontal plane can serve as a measurement of apparent displacement, which is different from the true displacement of the slip line in a 3D model (Tapponnier abd Molnar , 1976; Williams and Vann, 1987; Shaanan et al., 2014; Zielke et al., 2015; Fossen and Rotevatn, 2016). To reduce the influence of this difference, we must convert the true displacement from the apparent displacement of the slip line of two intersecting faults, and then calculate its true pitch angle according to the geometric relationship between the two faults.

Branch faults commonly develop on both sides of a master fault in both extensional and strike-slip settings (Harding, 1974; Benesh et al., 2014). The Riedel shear model describes a characteristic pattern of secondary fractures (e.g. R, R', P shears) that develop in a brittle medium under simple shear stress, mimicking the geometry of natural strike-slip fault zones (Riedel, 1929; Dooley and Schreurs, 2012; Fossen, 2016). Concurrently, the strike-slip strain ellipse model proposed by Harding explains the systematic distribution of extensional, contractional, and strike-slip structures around a master fault based on the rotation of the principal stress axes (Harding, 1974). Noting the above observations, this study analyzes the geometric characteristics of these branch faults within the framework of the Riedel shear model, adopting its fundamental geometric and kinematic framework where secondary faults form at predictable angles

to the master fault under a regional simple shear regime. At the same time, the right-lateral strike-slip strain ellipse model is introduced as a constraint for the regional geological background. This model's framework, which partitions deformation into specific quadrants of extension and transcurrent motion, provides the foundational stress state for establishing our new geometric model in the JYD. By analyzing the attitudes of the fault zones in the regional extension-strike-slip composite stress field, we can simplify and establish a fault zone model under the condition that the homogeneous fault-blocks undergo rigid body motion along the fault. Given this, the intersection points on both walls of intersecting faults at the studied horizon (or a certain reflection interface) are taken as piercing points according to the idea of matching facies or other distinctive geological features (Fig. 3a, b; Chen et al., 2024). In Fig. 3b, the slip line (green line) is that made by the intersection of two faults (master and branch), and the two ends of the green line are the intersections of the line and a certain stratigraphic surface on the hanging wall and the footwall. These two points at either end of the slip line are what define the all-important piercing points. Ideally, quantitative determination of the kinematic properties of such faults can be achieved with detailed data of fault displacement components, allowing calculation of the pitch angles of these faults and the geometric relationships between master faults and branch faults. Alternatively, if it is not possible to calculate the displacement components via piercing points, stereographic projection analysis can be used for quantitative analysis, as long as the strike and dip angle of each fault is known (Fig. 3c).

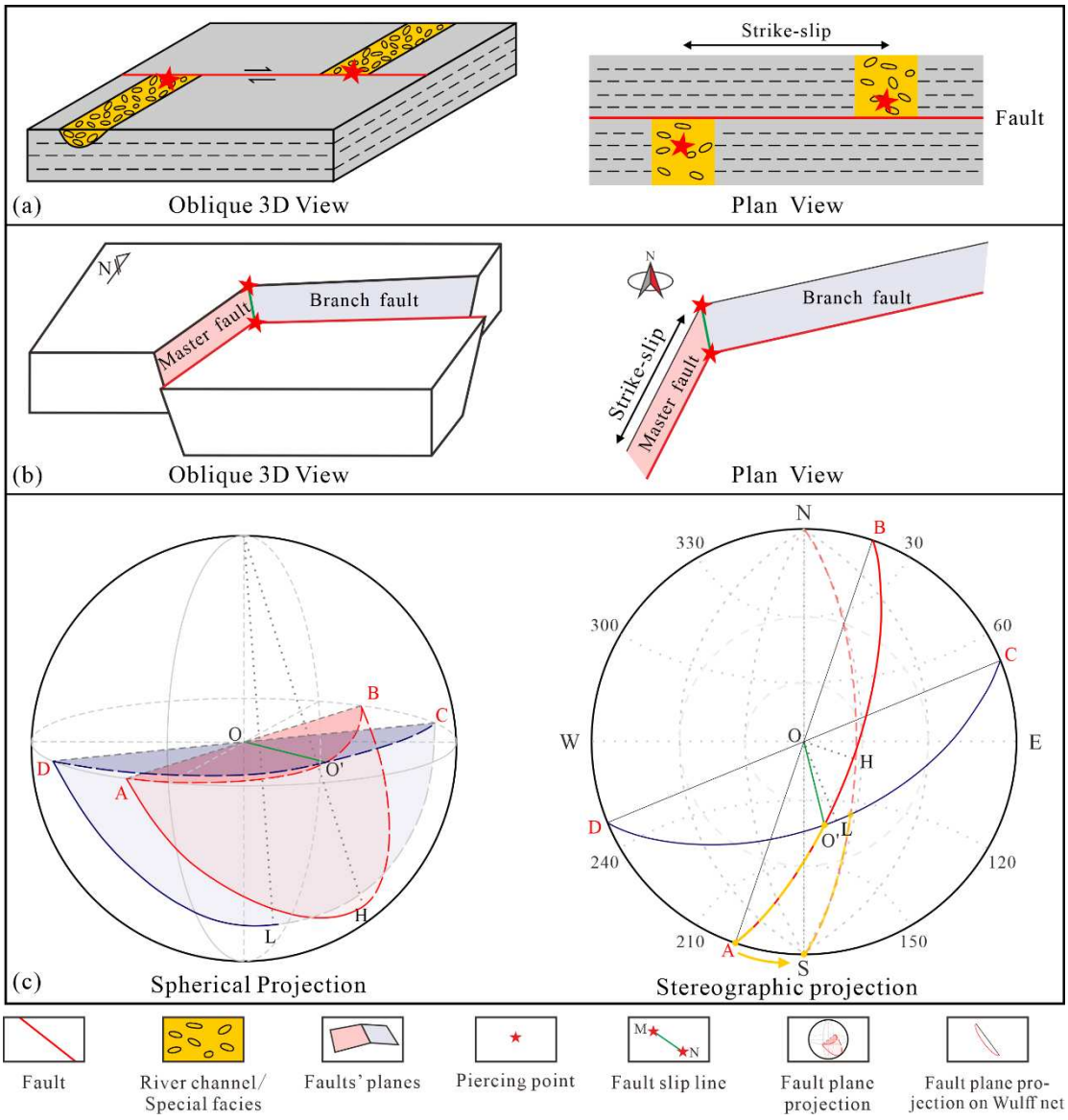

Fig. 3. Principles of piercing points used to determine offset across faults and two quantitati analytical methods

(a) Two views of the method to constrain minimum fault slip that requires the location of piercing points by pairs of matching sedimentary facies on both sides of the fault (according to Waldron et al., 2015). (b) A novel model for locating piercing points across intersecting faults for a certain stratigraphic surface; the conversion of fault kinematics parameters between an oblique 3D view and plan view is also the main concept of the geometric quantitative calculation method. (c) Lower hemisphere projection of two fault planes $\overset{\frown}{CFD}$ and $\overset{\frown}{AEB}$ (e.g. the master and branch fault planes in Fig. b) on the projection sphere (left) and on the Wulff net (right).

3.1. A novel geometric model for combinations of fault zones

In structural belts with lateral branch faults, where the principal displacement zone (PDZ) developed in an extension-strike-slip area bends along its strike, a series of oblique, scattered lateral, or horsetail secondary faults commonly develop at the tip of the master fault (Dooley and Schreurs, 2012). In a fault zone that has experienced multiple stages in the evolution of stress, the dip displacement component of the master fault generally reflects superposition of extension and compression in this area, and the sum of the dip displacement components of the branch faults on each side of the master fault reflects the strike displacement component of the master fault, that is, the strike-slip displacement component of the fault zone. Accordingly, this model divides the branch faults into two cases, which are respectively located at the end and in the lateral part of the master fault (Fig. 4a, c), with their corresponding 2D plane projection modes (Fig. 4b, d). In summary, the principle of modelling a fault zone is actually to combine these two conditions according to the actual development of the fault zone. The simplest model is that two branch faults develop, one at each tip of the master fault. Otherwise, in addition to these two branch faults, one or more branch faults may also develop in the lateral part of the master fault.

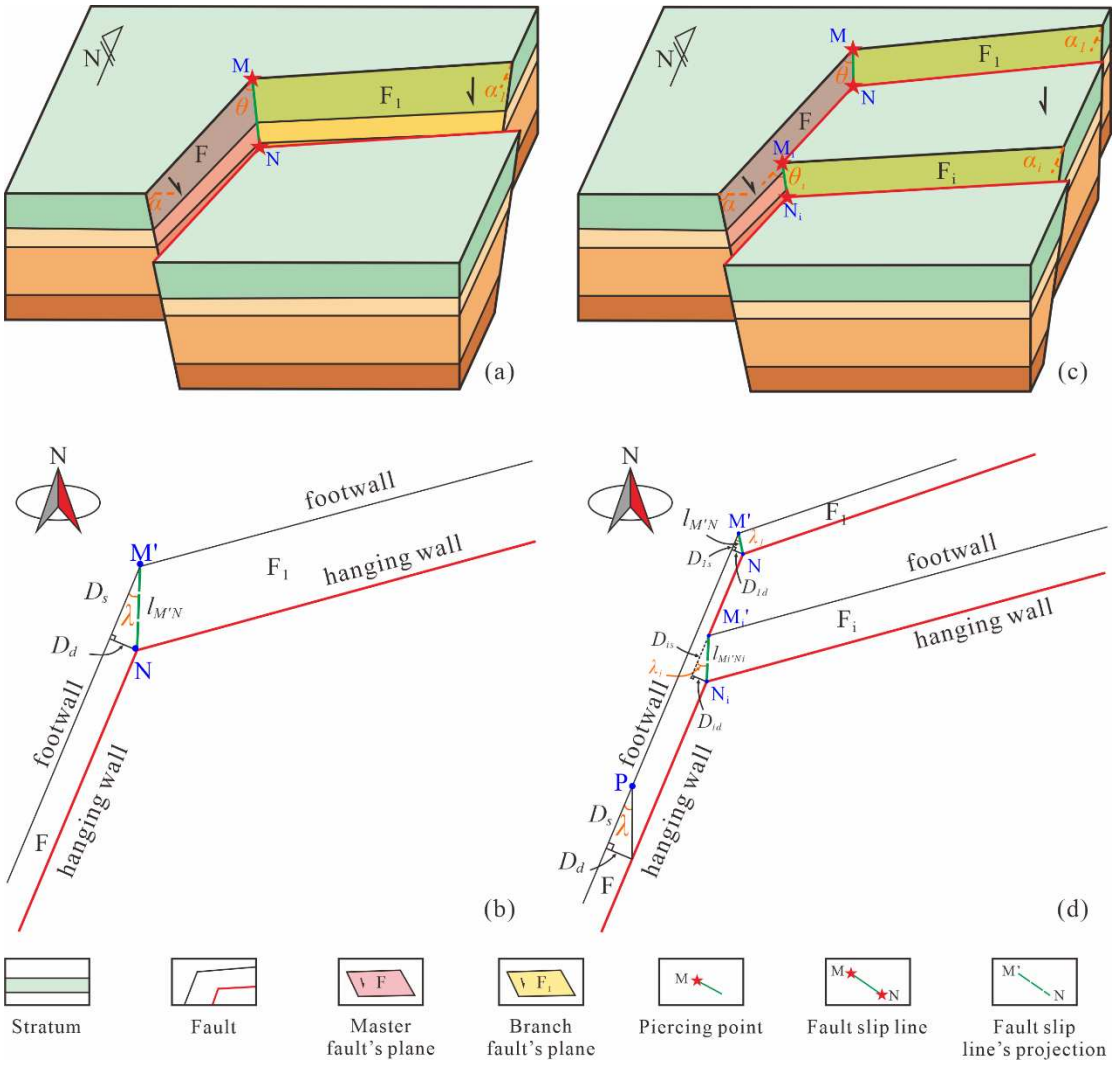

Fig. 4. Schematic geometric model and plane projection of fault zones at the fault intersection.

α- the dip ; θ - true pitch angle; $l_{M'N}$ - the true length (l) of M′N; D_d - the dip-slip component of MN along F; D_s - the strike-slip of MN along F; λ - the apparent pitch angle between F and M′N. (a) 3D model of intersection of one end of a master fault intersecting a single branch fault; (b) plane projection of model (a); (c) 3D model of intersection of one end of a master fault intersecting multiple branch faults; and (d) plane projection of model (c).

MN – the fault slip line at the intersection between the branch fault and F (on 3D model); M′N – the fault slip line's horizontal projection (on 2D model); $l_{M'N}$ - the true length of M′N; D_d - the horizontal component of dip slip of MN along F; D_s - the horizontal component of strike slip of MN along F; λ - the apparent pitch angle between F and M′N; M_iN_i - the fault slip line at the intersection between the corresponding branch fault (F_i) and F (on 3D model); $M_i'N_i$ - the fault slip line's horizontal projection of M_iN_i (on 2D model); D_{id} - the dip slip component of M_iN_i along F; D_{is} - the strike slip of M_iN_i along F.

According to the fault coherence principle (Mouslopoulou et al., 2007), the azimuth and magnitude of the strike and dip-slip of a particular fault vary continuously with the strike direction, but their vector sum remains constant, meaning that the horizontal slip vector remains unchanged. Assuming brittle deformation and rigid body motion, the total slip distance of the piercing point at any position along the fault remains constant. This consideration disregards the plastic deformation of the strata and the energy absorbed during fault fracture. It is acknowledged that the causes and mechanisms of rock plastic deformation are complex, requiring detailed analysis of the dynamic mechanisms and calculations. However, deformation induced by complex shear stress fields exhibits multi-solution nature. Given the difficulty in ensuring calculation accuracy under such deformation conditions, reliable quantification of deformation effects requires detailed constraints on stress orientation and intensity. Specifically, without these constraints, assessing fault-block deformation's impact on strike-slip and dip displacement components becomes unreliable, thus amplifying errors in the displacement calculated through piercing points. Based on this theoretical framework, the kinematically relevant parameters obtained from the structure plan or other related diagrams like the ant-tracking attribute volume can be converted into three-dimensional space. This approach significantly streamlining the research process while preserving critical characteristics of fault zone development, Thus, the true total displacement of the master fault in various cases can be approximately calculated based on this theory, and then the kinematic property of the fault zone can be identified quantitatively.

3.2. Quantitative calculation method of fault geometry

In cases where the piercing points of the hanging wall and footwall of the fault can be established, kinematic parameters related to the projection of the fault slip line can be computed in the structural plane (i.e., the plan view of the fault) of a 2D model. These parameters enable the conversion of the true pitch angle (θ) in 3D space, facilitating the precise identification of the kinematic properties of the fault.

3.2.1. Calculation of pitch angle

$$D_d = l_{M'N} \cdot sin\lambda \quad \text{Eq. (1)}$$

$$D_s = l_{M'N} \cdot \cos\lambda \quad \text{Eq. (2)}$$

Where one end of the master fault (F) intersects with only one branch fault (F_1) on the same plane (Fig. 4a), the piercing points M and N on the footwall and hanging wall, respectively, are where branch faults F_1 and F intersect. Connecting these points forms the slip line (MN), with its horizontal projection being the component of the slip line (M′N) (Fig. 4b). Notably, several parameters in Eq. (1) and (2) are involved in determining apparent displacement components: $l_{M'N}$, represents the true length (l) of M′N; D_d, indicating the dip-slip component of MN along F; D_s, denoting the strike-slip of MN along F; and λ, signifying the apparent pitch angle between F and M′N. In the

plane projection of the model, obtaining the dip-slip and strike-slip components of the fault are straightforward, and calculating the λ of the M′N through Eq. (3) facilitates the identification of its apparent kinematic properties (Fig. 4c, d).

$$\lambda = \arctan\frac{D_d}{D_s} \qquad \text{Eq. (3)}$$

Although apparent pitch angle (λ) may not precisely represent the true kinematic property of the fault, the true pitch angle (θ) between MN and F can be derived from the 3D model (Fig. 5, Eq. (4)). In the following Eq. (4), α represents the dip angle of F.

$$\theta = \arctan\frac{D_o}{D_s} = \arctan\frac{\tan\lambda}{\cos\alpha} = arctan\frac{D_d}{\cos\alpha \cdot D_s} \qquad \text{Eq. (4)}$$

When true pitch angle (θ, Eq. (5)) falls within the range of $0°<\theta<45°$, F is characterized by strike-slip dominance. Conversely, when it ranges from $45°<\theta\leq90°$, F indicates dip-slip dominance. As depicted in Fig. 4a and 5, in cases where F is a strike-slip fault or a normal strike-slip fault, certain conditions must be met:

$$\tan\theta = \frac{D_o}{D_s} < 1 \qquad \text{Eq. (5)}$$

In the model depicted in Fig. 4c, one end of F intersects multiple branch faults. M_iN_i represents the fault slip line at the intersection between the corresponding branch fault

(F_i) and F, and its horizontal projection slip line is $M_i'N_i$ (Fig. 4d). Similarly, the relationship between the apparent pitch angle (λ_i, Eq. (6)) and slip of M_iN_i along F can be determined.

$$\lambda_i = \arctan\frac{D_{di}}{D_{si}} \qquad \text{Eq. (6)}$$

As shown in Fig. 4d, D_{di} is the dip-slip component of M_iN_i along F and D_{si} is the strike-slip component of M_iN_i along F.

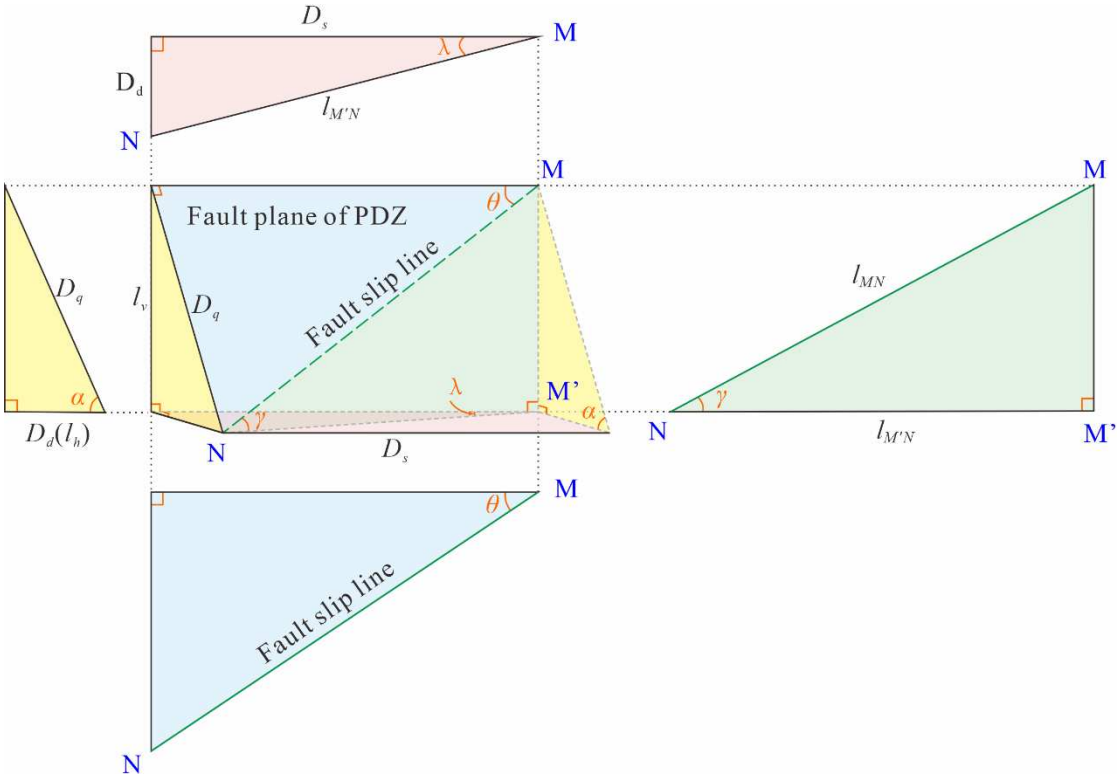

Fig. 5. Schematic diagram of trigonometric function relationship conversion of fault related parameters in 2D and 3D space.

α - the dip of F; θ - true pitch angle; λ - the apparent pitch angle; γ - plunge angle.

Owing to the variations in the strike, dip (α, Fig. 5), and scale of each branch fault, the pitch angle (θ, Fig. 5) of a single branch can only represent the local kinematic property of the fault at that piercing point. To more comprehensively characterize the properties of the whole (e.g. a certain point P in Fig. 4d) of the master fault, defining the comprehensive apparent pitch angle (λ) as the characterization parameter of the cumulative strike-slip and dip-slip distances of the activity of a series of branch faults at one end of the master fault on the horizontal projection, and the comprehensive true pitch angle (θ) is required. Therefore, it is essential to calculate the cumulative displacement components (D_d and D_s at point P) of F_i in Eq. (7) and (8), considering its movement along both the dip and strike of F.

$$D_d = \sum_{1}^{n} D_{di} = \sum_{1}^{n} l_{Mi'Ni} \cdot \sin\lambda_i \quad \text{Eq. (7)}$$

$$D_s = \sum_{1}^{n} D_{si} = \sum_{1}^{n} l_{Mi'Ni} \cdot \cos\lambda_i \quad \text{Eq. (8)}$$

Among these, $l_{Mi'Ni}$ is the true length of $M_i'N_i$.

Substituting cumulative strike-slip displacement component (D_d) and cumulative dip displacement component (D_s) into Eq. (3) yields the comprehensive apparent pitch angle (λ) of F. Subsequently, θ can be calculated using Eq. (4) to identify the kinematic properties of F. By introducing the concept of cumulative displacement components,

this method can consider the differences in the contribution of branch faults to the tectonic activities of a fault zone, thereby reducing the potential errors caused by the weight allocation for each branch fault.

3.2.2. Calculation of fault dip angle

As depicted in Fig. 6, this work presents two methods for calculating the fault dip angle. In the cross-section of the depth domain parallel to the fault dip (Fig. 6a), the angle α can be directly measured at the corresponding reflector (stratigraphic horizon) (Fig. 6b), or by determining the horizontal separation (l_h) and vertical separation (l_v) of the fault at a specific reflector (stratigraphic horizon) in the depth domain. It is noteworthy that this can only be done accurately if the seismic data are available in the depth domain and if the applied velocity model used for time to depth conversion is reliable. Furthermore, in the structural plane corresponding to the reflector (stratigraphic horizon), two contours intersecting the fault-plane are located, and their intersection points are connected (Fig. 6c). Subtracting the elevations of the two points yields the value of l_v from which l_h can be calculated. Finally, α can be determined using Eq. (9).

$$\alpha = \operatorname{acrtan}\frac{l_v}{l_h} \qquad \text{Eq. (9)}$$

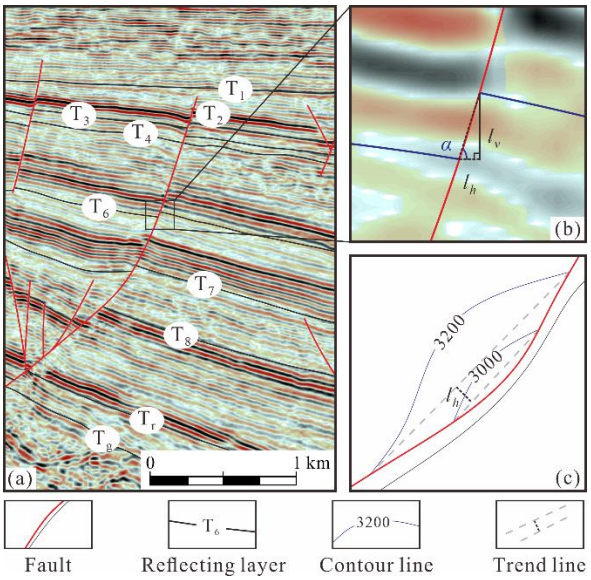

Fig. 6. Schematic diagram of the calculation method of fault dip angle in depth domain seismic data.

3.3. Stereographic projection method

The stereographic projection method is commonly employed in structural geology to analyze fault attitude and slip distances (Koons et al., 2003; Benesh et al., 2014). Additionally, this method can analyze plunge angle (γ) and true pitch angle (θ) of MN by projecting the attitudes of both the master fault and branch faults. Each projection result precisely reflects the kinematic properties of F at its intersection with the analyzed branch fault (F_i) in Fig. 4a. Notably, branch faults that develop simultaneously in each fault zone commonly exhibit a certain regularity in size and attitude, indicated by the proximity (or a difference of 180°) in their attitudes. Consequently, the attitude of fault slip lines where branch faults intersect F are similar. Where multiple branch faults are present, the fault attitudes of the master fault and each branch fault may be individually measured and projected onto a projection sphere. Analyzing the plunge angle (γ_i) of each fault slip line allows the identification of the local or global kinematic

properties of the fault zone based on the corresponding value of θ_i or regionally based on the average θ_i of several branch faults in a certain area (usually at one end of the master fault), respectively. Alternatively, we can stipulate that the pitch angle of the branch fault with the largest scale or displacement on the same side of the master fault is taken as the representative value.

The projection method may use either a Wulff net, a Lambertian equatorial net, or a Schmidt equal-area net; however, a Wulff net is most commonly used (Howarth, 1996). In this study, a Wulff net was employed in the analysis with the stereographic projection method. Initially, the stratigraphic horizon under analysis was determined, followed by plotting the attitudes of intersecting faults (both master and branch faults) on this horizon using the Wulff net. Subsequently, the two arcs representing the cross-section attitudes intersect at point (O′) on the sphere (Fig. 3c). By connecting the centre of the Wulff net (O) with point O′, the value of the line OO′ projected on the longitudinal line of the Wulff net represents the strike of the fault slip line (MN), and the value of it projected on the latitude line denotes the dip angle of MN, which is defined as the plunge angle (γ). Finally, this method provides two approaches to determine the pitch angle (θ) of MN on the master fault. (1) Directly reading the angular distance of the dark yellow dashed arc in Fig. 3c - stereographic projection, which is the pitch angle. This is achieved by rotating the arc $\overset{\frown}{\mathrm{AO'B}}$ around the Wullf net centre until its endpoints coincide with the north and south poles; the latitude reading at point O′ then

gives the angular distance. (2) In addition, the true pitch angle (θ) of MN can be calculated using Eq. (10) and (11).

$$\cos\theta = \cos\lambda \cdot \cos\gamma \quad \text{Eq. (10)}$$

$$\sin\theta = \frac{\sin\gamma}{\sin\alpha} \quad \text{Eq. (11)}$$

The results derived through the stereographic projection method yield the kinematic characteristics of the fault at a specific location along the master fault. The local kinematic properties of F may be different due to the heterogeneity of lithology and stress. Where multiple branch faults are developed on one end of F, the local kinematic properties that intersect with the branch faults can be varied. Therefore, to accurately depict the stress and development characteristics of a master fault, it may be essential to analyze the attitudes (including γ_i) of fault slip lines related to all branch faults at one end of F.

3.4. Identification of kinematic properties

For simplicity, the apparent strike-slip property can be determined based on the attitude of the horizontal component of slip line at the intersection of F and a branch fault in the structural plane. However, the true strike-slip property of the fault is identified using θ. Based on the criteria in Eq. (5), it can be further classified as follows: A fault with $0°<\theta<10°$ is categorized as a strike-slip fault; $10°<\theta<45°$ is a normal strike-slip fault;

$45° < \theta < 80°$ is a strike-slip normal fault; and $80° < \theta \leq 90°$ is a normal fault (Liu, 1993; Chen et al., 2022).

Notwithstanding, the results of the algorithm reflect the comprehensive kinematic properties of cumulative tectonic activity over a certain period from the beginning of fault activity to the target horizon. However, they may not directly capture kinematic properties over short geological timeframes, which requires simultaneous calculation and comparison of fault kinematic properties at the top and bottom interfaces over this depositional period. The kinematic properties of a fault zone over a brief period can be depicted more accurately if its corresponding displacement components in the two sets of reflectors (horizons) can be acquired.

3.5. Data

The study utilized three-dimensional (3D) seismic data provided by the Shengli Oilfield Company, Sinopec, which covers an area of 2.55×10^4 km^2. Inline, crossline and vertical geometric sample intervals were 30 m, 35 m and 2 ms, respectively. The dominant frequency of the seismic data is about 35 Hz. The original time-domain seismic data was converted into depth-domain seismic data using 2DMove software.

Horizon standardization and systematic interpretation of 3D seismic data were conducted using Petrel. Specifically, eight key Cenozoic stratigraphic horizons (Fig. 2,

T_r, T_7, T_6, T_4, T_3, T_2, T_1, T_0) were interpreted, and the presence of key fault zones of the JYD were identified. According to the structural plane, the reflection interface of T_2 and T_6 were locked, and correspond to true geological horizons at the base of the E_3s_1 and $E_2s_3^L$ sub-members, respectively. In addition, 3D seismic cross-sections were used to explain the presence of faults in the formation.

4. Results

4.1. Method 1: quantitative calculation method of geometry

4.1.1. Changdi fault zone: The pattern of a single branch fault at one end

Using the kinematic properties of the Changdi fault zone (F_2) as an illustration (Fig. 1), the fault extends in an S-shape at the base of $E_2s_3^L$ (Fig. 7a). Adjacent to F, only one branch fault develops on each side, sequentially labeled as sections F_1 and F_1' from east to west (Fig. 7b).

At the intersection of F and F_1 (Fig. 7c), the true length of M'N measures 1.13 km with an apparent pitch angle (λ) of 24.12°. Utilizing Eq. (1), (2), and (9), D_s and D_d of M'N along F, alongside the dip (α) of F, are calculated as 1.03 km, 0.46 km, and 56.06°, respectively. By substituting these parameters into Eq. (3), (4), it can be concluded that λ and θ of the fault slip line MN on the master fault were 24.12° and 38.72°, respectively (Table 1). Thus, F is identified as a normal strike-slip fault, with the strike-slip movement predominantly influencing the fault evolution since the $E_2s_3^L$ depositional

period.

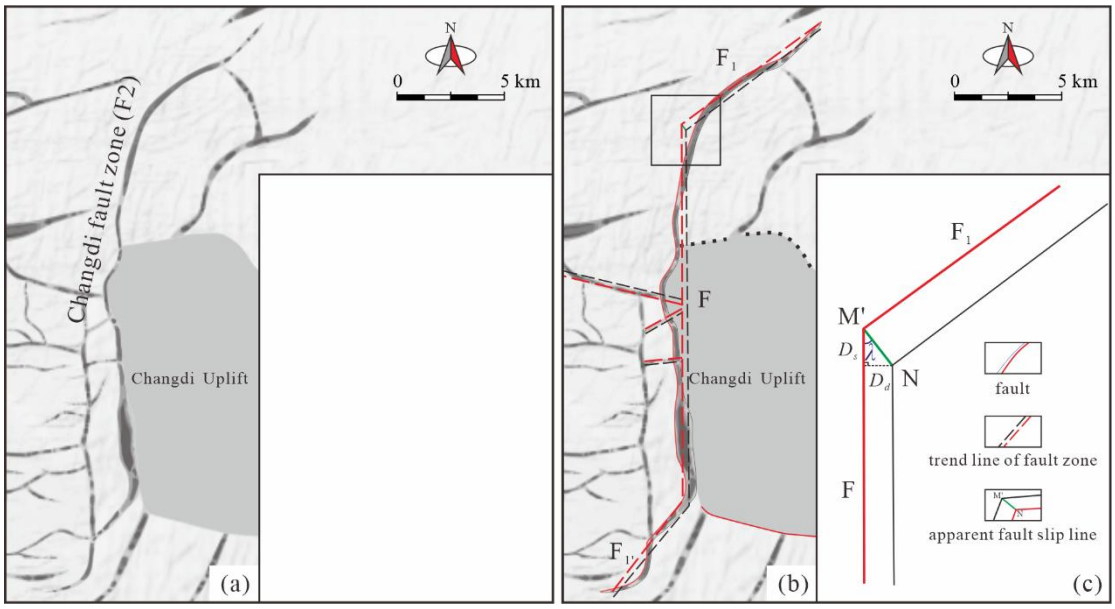

Fig. 7. Uninterpreted coherence slice (a), interpreted fault plane (b) and local magnification model at the intersection (c) of the Changdi fault zone at the base of $E_2s_3^L$

Table 1 Statistical table of kinematic property identification results of key fault zones in Jiyang Depression at the base of $E_2s_3^L$ by Method 1

Num	Strike slip D_s/km	Oblique slip D_o/km	Tendency/°	Dip/°	Apparent λ/°	True θ/°	Kinematic property
1	1.14	0.88	222.19	56.06	23.28	37.60	Extension-strike-slip
2	1.03	0.82	270.01	56.04	24.12	38.72	Extension-strike-slip
3	0.92	0.78	276.08	60.16	21.37	38.18	Extension-strike-slip
4	1.73	1.07	294.40	52.63	20.57	31.72	Extension-strike-slip
5	0.75	1.86	237.89	59.73	51.50	68.00	Strike-slip-extension
6	0.76	1.49	137.78	64.10	40.73	63.10	Strike-slip-extension
7	1.80	3.83	119.30	72.95	31.91	64.79	Strike-slip-extension
8	0.69	1.02	112.18	70.02	26.90	56.03	Strike-slip-extension
9	0.37	0.44	123.95	44.75	39.76	51.52	Strike-slip-extension
10	2.18	2.16	300.21	66.88	21.26	44.79	Extension-strike-slip
11	3.52	3.36	142.64	62.85	23.55	43.69	Extension-strike-slip

4.1.2. Linshang fault zone: The pattern of multiple branch faults at one end

The Linshang fault zone (F_{11}) exemplifies this pattern (Fig. 8a). At the base of $E_2s_3^L$, four branch faults emerge on the east side and two on the west side of F. The northernmost branch fault on the east side is labeled F_1, followed by three successive branch faults (F_2–F_4) to the south of F_1 (Fig. 8b). These three are all secondary branch faults likely resulting from tension during fault activity, intersecting with F but are one-third the size of F_1.

From the structural plane and seismic profile at the base of $E_2s_3^L$, the strike and dip of F were 52.64° and 142.64°, respectively. The α registers at 62.85°, with $M_1'N_1$ at the F-F_1 intersection spanning 3.84 km (Fig. 8c, d). Utilizing Eq. (7), (8), and (11), the cumulative strike-slip (D_s) and cumulative horizontal component of dip-slip (D_d) of the northern F section are 3.52 km and 1.53 km, respectively. By applying these parameters to Eq. (3) and (4), λ and θ of MN were computed as 23.55° and 43.69°, respectively (Table 1), indicating that the Linshang fault zone is a normal strike-slip fault. Notably, the cumulative displacement components (D_s') and (D_d') of the two western branch faults of F are consistent with the equivalent values of the branch faults on the east side, registering at 3.57 km and 1.51 km, respectively. This final identification demonstrates the Linshang fault zone classification as a normal strike-slip fault zone.

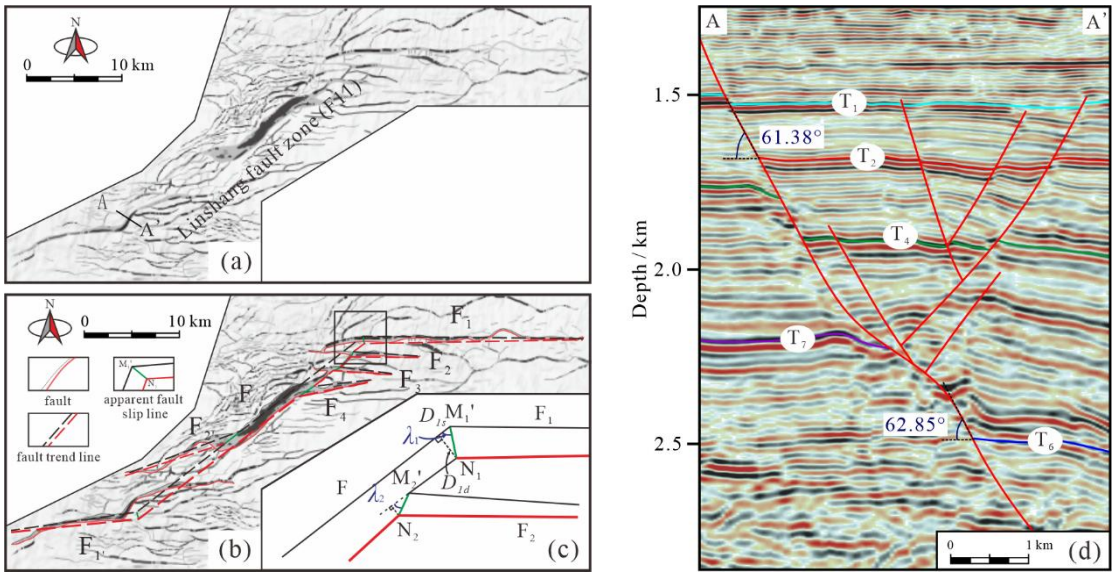

Fig. 8. Uninterpreted coherence slice (a), interpreted coherence slice (b), local magnification model at the intersection (c) and interpreted fault plane cross-section (d) of the Linshang fault zone at the base of $E_2s_3^L$

However, when evaluating the comprehensive kinematics of the master fault, spatial heterogeneity should be considered as the local kinematic properties may vary. For example, at the F-F_2 intersection ($M_2'N_2$ in Fig. 8), λ_2 is 28.82° and θ_2 calculated from Eq. (4) is 50.33°. This indicates a local strike-slip-normal fault kinematic character at F_2, which is inconsistent with the comprehensive characteristics of the fault zone and suggests segmented activity along the fault. In practical research, the choice between using the comprehensive pitch angle representing the entire master fault or the value representing a local segment should be based on the specific research objectives and requirements.

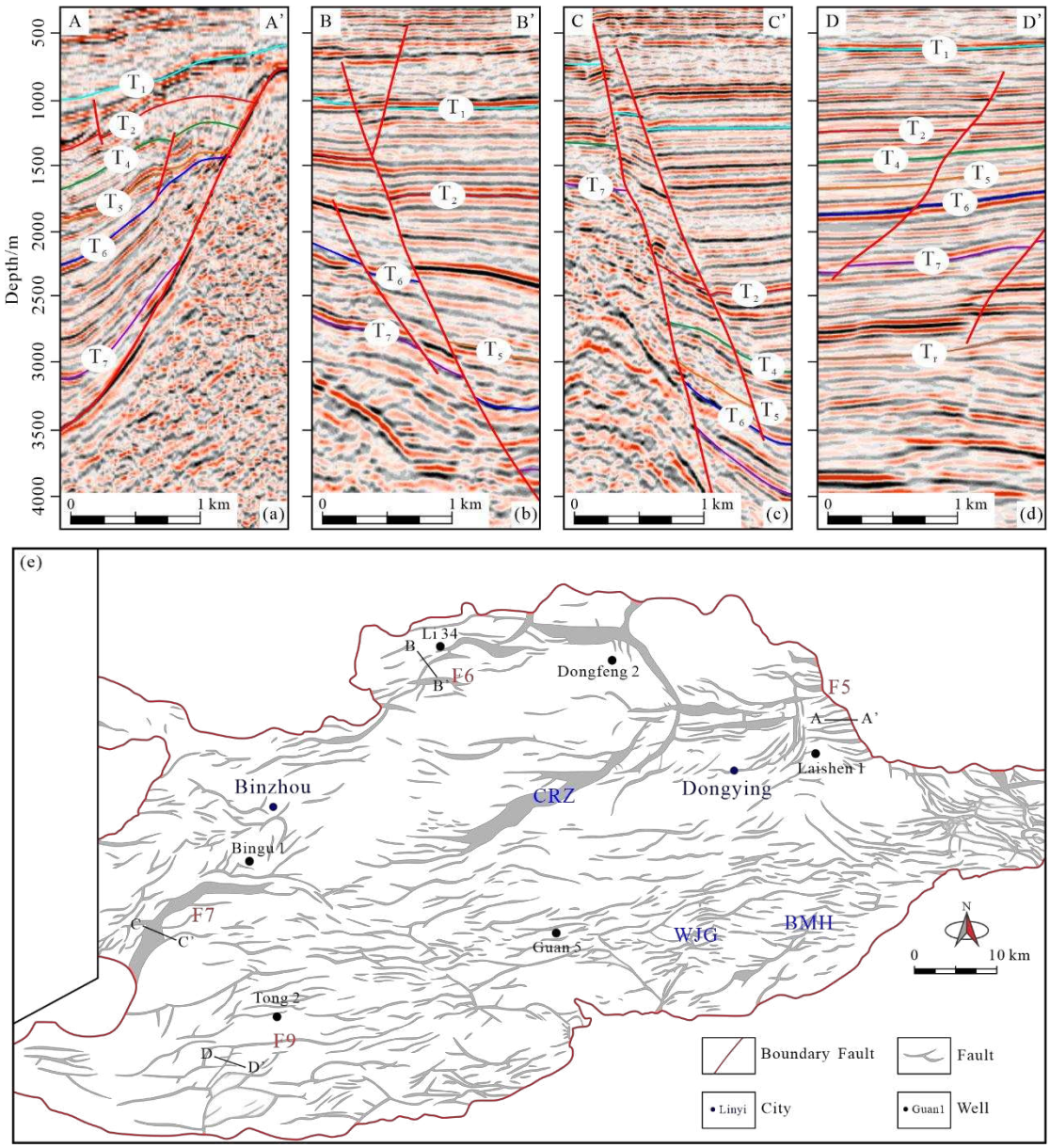

Fig. 9. Interpreted cross-sections of master faults (a-d) and the fault distribution plan of T_6 reflector (e) in Dongying Sag. CRZ – Centre rift zone, WJG – Wangjiagang fault zone, BMH – Bamianhe fault zone.

4.1.3. The calculation results of Method 1

Eleven major fault zones across the JYD were investigated. The relevant parameters of the two reflectors (T_2 and T_6) of the master fault zones can be calculated by interpreting the 3D seismic data in the depth domain (Fig. 9) through geometric relationships

between the master fault and brunch faults. According to the approach, we derived statistical Tables 1 and 2 to delineate the kinematic property identification results for the primary tectonic zones within the JYD at the base of the $E_2s_3^L$ (T_6 reflector) and E_3s_1 (T_2 reflector).

Table 2 Statistical table of kinematic property identification results of key fault zones in Jiyang Depression at the base of E_3s_1 by Method 1

Num	Strike slip D_s/km	Oblique slip D_o/km	Tendency/°	Dip/°	Apparent λ/°	True θ/°	Kinematic property
1	0.63	0.52	236.56	54.77	25.46	39.54	Extension-strike-slip
2	0.42	0.36	270.00	56.98	24.86	40.38	Extension-strike-slip
3	0.41	0.39	279.85	57.52	27.12	43.65	Extension-strike-slip
4	0.69	0.62	293.65	62.26	22.45	41.60	Extension-strike-slip
5	0.52	1.94	242.45	68.46	53.81	75.00	Strike-slip-extension
6	0.29	1.10	137.78	66.00	57.28	75.36	Strike-slip-extension
7	1.40	3.64	119.30	72.96	37.33	68.97	Strike-slip-extension
8	0.27	0.38	112.18	59.00	35.58	54.25	Strike-slip-extension
9	0.11	0.20	126.56	44.82	51.32	60.41	Strike-slip-extension
10	1.05	1.03	337.23	63.06	23.97	44.38	Extension-strike-slip
11	1.20	1.17	142.49	61.38	24.98	44.20	Extension-strike-slip

4.2. Method 2: stereographic projection method

4.2.1 Changdi fault zone: The pattern of a single branch fault at one end

Taking the Changdi fault zone (Fig. 7a) as an example, the attitudes of F_1 and F were 324.13° ∠ 32.06° and 270.00° ∠ 56.04°, respectively. These data were projected sequentially onto a Wulff net to obtain arcs $\overset{\frown}{AO'B}$ and $\overset{\frown}{CO'D}$ (Fig. 10). The point O′ represents their intersection, whereas the attitude of the OO′ denotes the plunge of the syncline and its plunge angle (γ) on the MN, measuring 335.66° ∠ 31.47°. By

employing Eq. (11), θ of MN was determined to be 39.01°. Alternatively, the pitch angle θ also can be read directly from the angular distance of point O' on $\overset{\frown}{CO'D}$ (the dark yellow dashed arc in Fig. 10) as 39.08° (Table 3). Consequently, the northern segment of the Changdi fault zone is interpreted as a normal strike-slip fault, at least since the $E_2s_3^L$ sedimentary stage, corroborating the results obtained through quantitative geometric analysis.

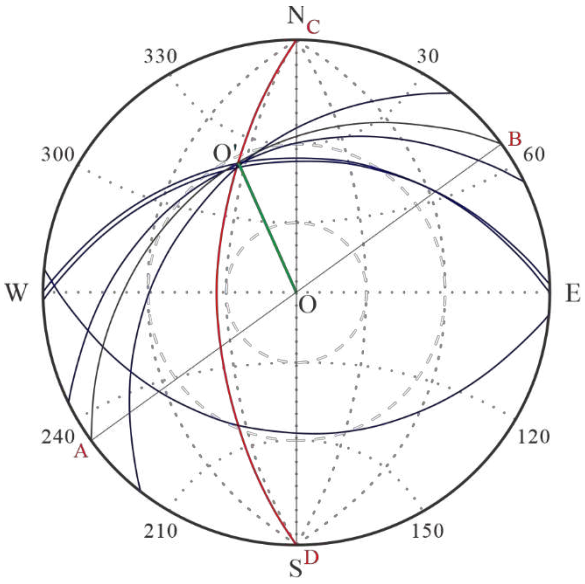

Fig. 10. Stereographic projection of master and branch faults of the Changdi fault zone at the base of $E_2s_3^L$.

The red arc line shows the projection of dip and dip angle of the master fault, black and dark blue arc lines indicate the projection of dip and dip angle of branch faults, and the green line (OO') represents the dip and dip angle of the intersection line between branch fault and the master fault, that is, the value of its latitude line is the local plunge angle (γ) of the master fault, which can be converted from Eq. (11) to get true pitch angle (θ). Same in Fig. 11.

4.2.2. Linshang fault zone: The pattern of multiple branch faults at one end

In the Linshang fault zone (Fig. 8a, 11), the branch faults on the same side of F typically

exhibit similar fault morphologies and developmental scales. Analyzing the attitude of the fault slip line at the juncture of F and each branch fault on the north end (F_1–F_4, Fig. 8b) facilitated the determination of their average pitch angle, serving as a representation of the kinematic attributes of the northern segment of the Linshang fault zone.

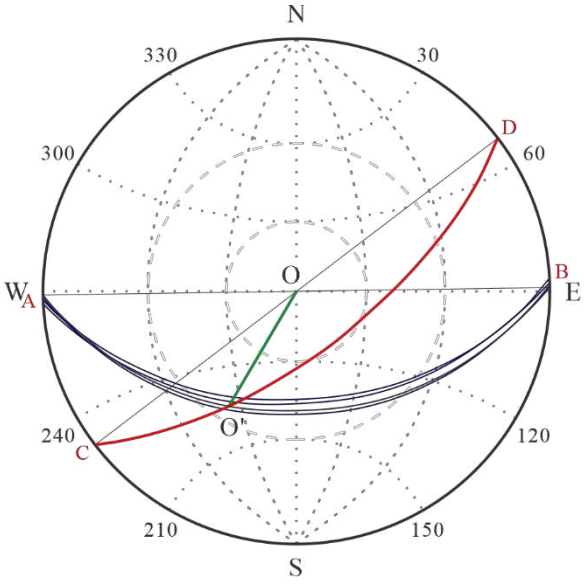

Fig. 11. Stereographic projection of master and branch faults of the Linshang fault zone at the base of $E_2s_3^L$.

The orientations of F_1 and F at the base of $E_2s_3^L$ were 179.03°∠34.22° and 142.64°∠62.85°, respectively. Subsequently, two fault-planes were successively projected onto a Wulff net, yielding arcs $\overset{\frown}{AO'B}$ and $\overset{\frown}{CO'D}$ (Fig. 11). This process enabled the determination of the attitude of the OO′, representing the plunge of the syncline and its plunge angle (γ_1) along the fault-slip line (M_1N_1), which measured 210.00° and 37.00°, respectively. The pitch angle (θ_1) of M_1N_1 was computed to be 42.56° (Table 3). Using the same methodology as in Section 4.2.1, the pitch angles (θ_2–θ_4) of F_2–F_4 were

determined as 45.63°, 42.83°, and 43.97°, respectively. Consequently, the average pitch angle (average value) of the northern segment of F was 43.75°, indicating that this section of the Linshang fault has functioned as a normal strike-slip fault since the $E_2s_3^L$ deposition stage, which is consistent with the findings obtained through quantitative geometric analysis.

4.2.3. The analytical result of Method 2

The attitude of the master faults and their associated branch faults within various tectonic zones in the JYD were individually projected onto the Wulff net. The analytical outcomes of the stereographic projection at the bases of $E_2s_3^L$ and E_3s_1 for each tectonic zone in the JYD are illustrated in Fig. 12, Table 3 and Table 4, demonstrating that the attitude of the branch faults in most tectonic zones are similar.

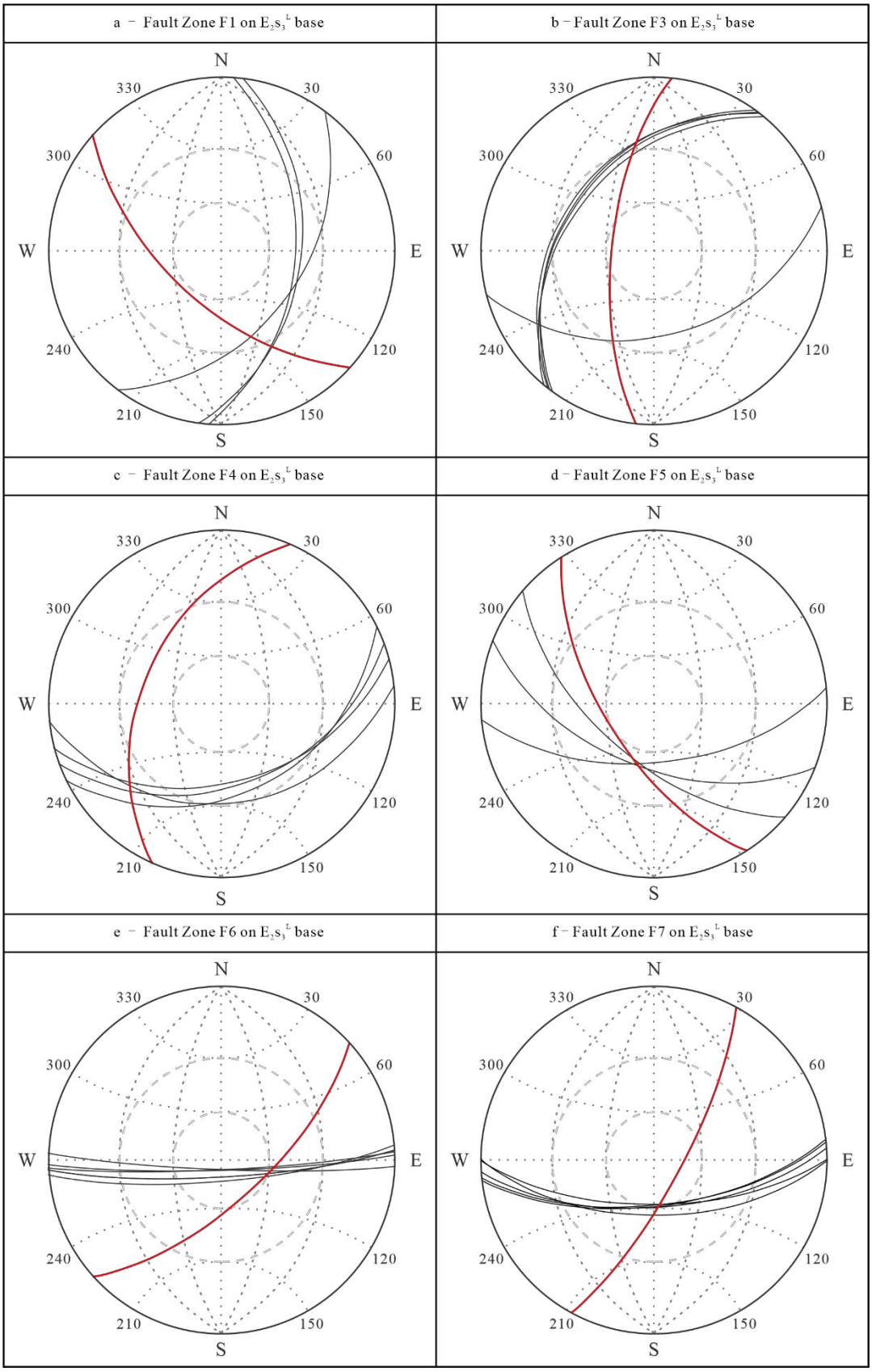

Fig. 12. Stereographic projection on $E_2s_3^L$ base and E_3s_1 base of fault zones in Jiyang Depression. The red arc line shows the projection of dip and dip angle of the master fault, black arc lines indicate the projection of dip and dip angle of branch faults

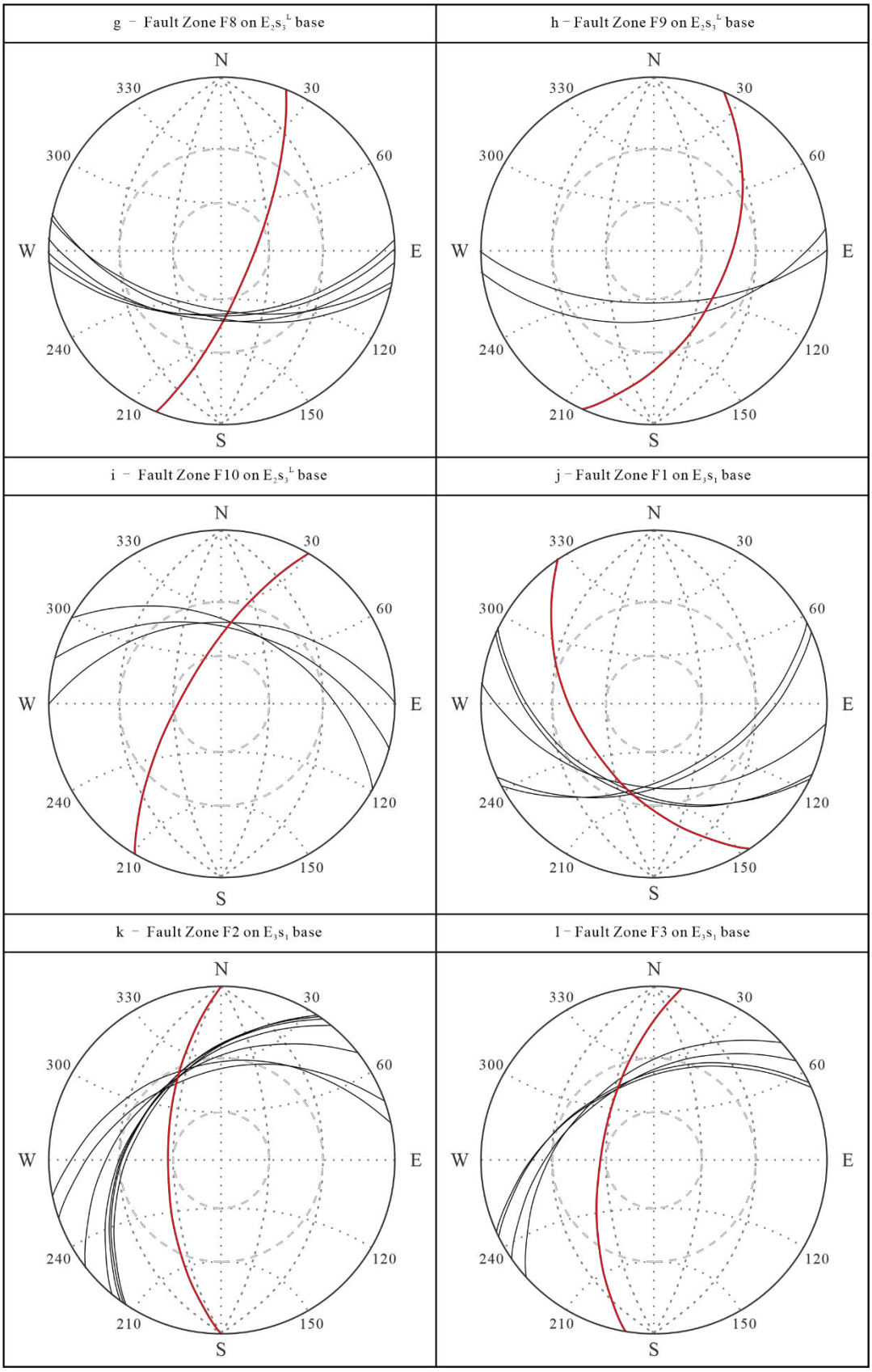

Fig. 12. Stereographic projection on $E_2s_3^L$ base and E_3s_1 base of fault zones in Jiyang Depression. (Continued)

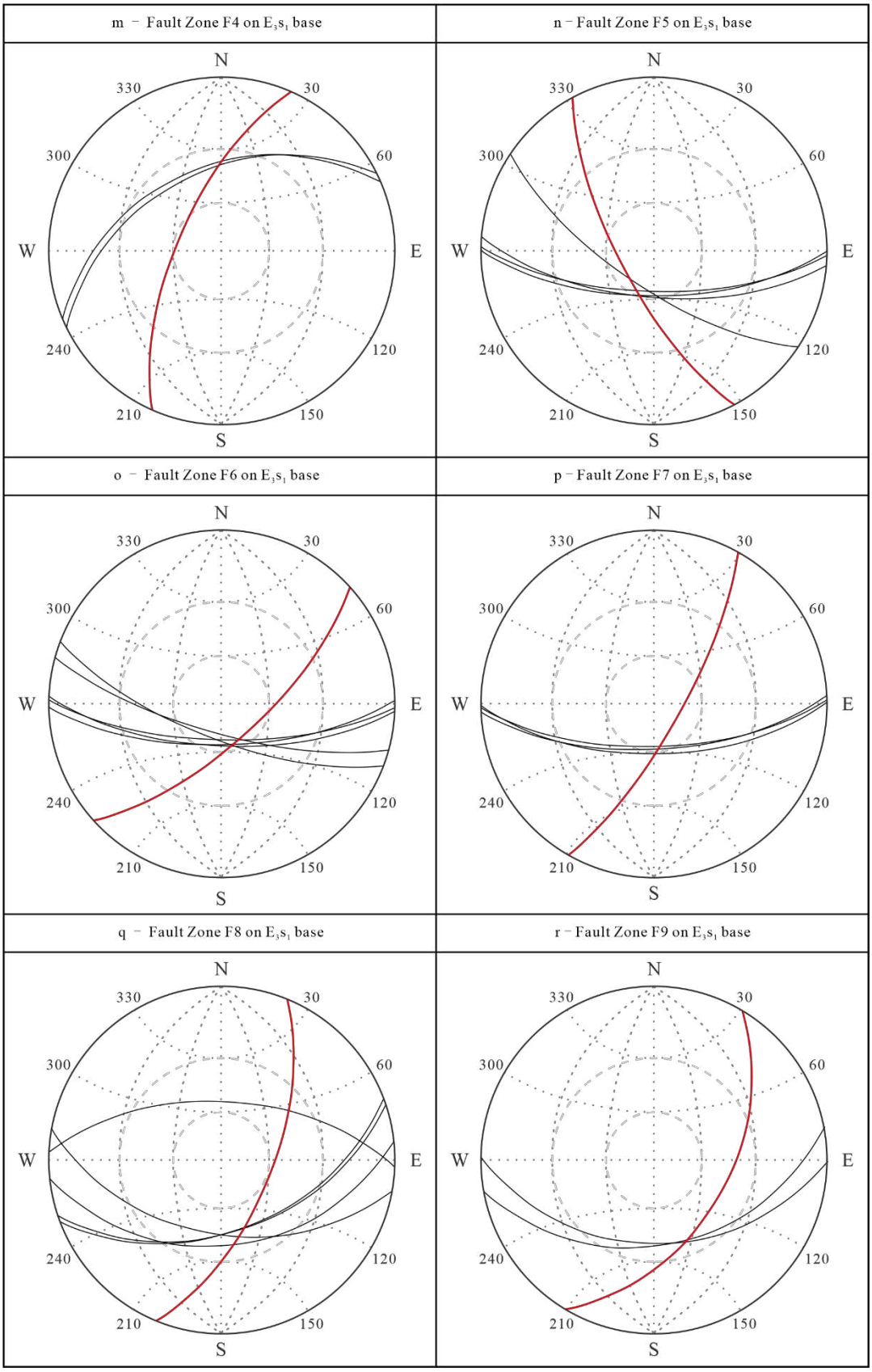

Fig. 12. Stereographic projection on $E_2s_3^L$ base and E_3s_1 base of fault zones in Jiyang Depression. (Continued)

Table 3 Statistical table of kinematic property identification results of key fault zones in Jiyang Depression at the base of $E_2s_3^L$ by Method 2 and the errors of true pitch angles between Method 1 (M1) and Method 2 (M2)

Num	Tendency /°	Dip/°	Plunge angle γ/°	θ by M1/°	θ by M2/°	Kinematic property	Error/ %
1	222.19	56.06	33.27	41.40	41.43	Extension-strike-slip	4.22
2	270.01	56.04	31.47	39.01	39.08	Extension-strike-slip	0.32
3	276.08	60.16	29.76	33.89	33.90	Extension-strike-slip	4.77
4	294.40	52.63	22.46	29.53	29.50	Extension-strike-slip	2.43
5	237.89	59.73	51.26	64.57	64.59	Strike-slip-extension	3.81
6	137.78	64.10	57.61	69.84	69.85	Strike-slip-extension	7.49
7	119.30	72.95	59.76	64.64	64.67	Strike-slip-extension	0.16
8	112.18	70.02	48.00	52.25	52.25	Strike-slip-extension	4.20
9	123.95	44.75	37.43	59.69	56.70	Strike-slip-extension	9.08
10	300.21	66.88	43.16	44.06	44.10	Extension-strike-slip	0.82
11	142.64	62.85	37.00	42.56	42.60	Extension-strike-slip	1.25

Table 4 Statistical table of kinematic property identification results of key fault zones in Jiyang Depression at the base of E_3s_1 by Method 2 and the errors of true pitch angles between Method 1 (M1) and Method 2 (M2)

Num	Tendency /°	Dip/°	Plunge angle γ/°	θ by M1/°	θ by M2/°	Kinematic property	Error/ %
1	236.56	54.77	33.27	37.08	37.10	Extension-strike-slip	2.73
2	270.00	56.98	31.47	43.75	43.75	Extension-strike-slip	3.74
3	279.85	57.52	29.76	41.39	41.40	Extension-strike-slip	2.51
4	293.65	62.26	22.46	45.48	45.47	Strike-slip-extension	4.31
5	242.45	68.46	51.26	72.42	72.40	Strike-slip-extension	2.87
6	137.78	66.00	57.61	79.84	79.85	Strike-slip-extension	5.04
7	119.30	72.96	59.76	65.26	65.30	Strike-slip-extension	4.13
8	112.18	59.00	48.00	46.19	49.20	Strike-slip-extension	8.96
9	126.56	44.82	37.43	60.11	60.10	Strike-slip-extension	0.33
10	337.23	63.06	43.16	43.31	43.30	Extension-strike-slip	1.19
11	142.49	61.38	37.00	40.29	40.30	Extension-strike-slip	4.34

5. Discussion: Methods and regional geological analysis

5.1. Statistics and analysis of kinematic parameters

Based on the above quantitative results and considering studies of en echelon strike-slip faults in the Dongying Sag, such as the Wangjiagang fault zone (WJG in Fig. 9; Yuan et al., 2022), the JYD can be divided into three regions (Fig. 13): Region A in the eastern sector of the depression, constitutes a normal strike-slip tectonic system close to the Tan-Lu fault zone, encompassing the northeastern Zhanhua Sag and the eastern Dongying Sag; Region B located in the central area of the JYD forms a strike-slip normal fault tectonic system flanked by two fault zones, comprising the entire Chezhen Sag, as well as the western portions of the Zhanhua and Dongying sags; and Region C, represented by the Huimin Sag in the western sector, constitutes a normal strike-slip tectonic system proximal to the Lan-Liao fault zone.

Most of the faults in Region A are NNE-striking, and their true pitch angle (θ) values of fault zones at the base of $E_2s_3^L$ and E_3s_1 ranged from 35° to 45°, except for F_5 in Table 1, 2. The fault F_5 shows more normal fault characteristics, which may be related to the connection of the regulating faults in the northeast of F_6 and the Centre Rift Zone (CRZ in Fig. 9). Whereas in Region C, θ ranges from 40° to 45°. Therefore, the primary faults within these zones were identified as normal strike-slip faults. In contrast, the θ values for the fault zones in Region B range from 45° to 80°, all exceeding 45°, indicating their classification as strike-slip normal faults.

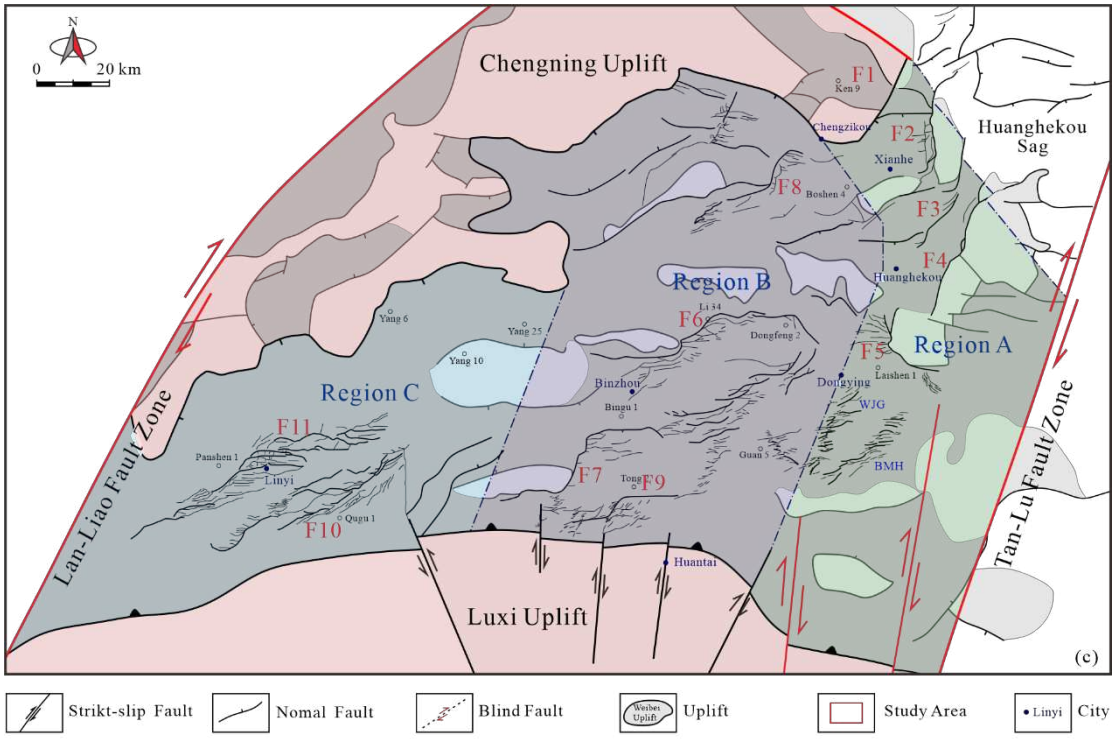

Fig. 13. Tectonic system division map of Jiyang Depression.

5.2. Analysis of tectonic activity during the E_3s_2-$E_2s_3^L$ sedimentary period

The strike-slip displacement components of T_2 and T_6 reflectors were selected for kinematic analysis due to their optimal quality and regional continuity in seismic data across the JYD. Movement between these reflectors captures the E_3s_2 - $E_2s_3^L$ sedimentary period, a critical phase of right-lateral strike-slip in the Bohai Bay Basin during the late Eocene to early Oligocene (Yuan et al., 2022). Kinematic characteristics during this interval are summarized as follows. (a) Region A, situated near the Tan-Lu fault zone (Fig. 13), comprises 6 fault zones (including WJG and BMH) with a strike similar to that of the Tan-Lu fault zone, along with the NW-striking F_5 fault. During the

Es3 sedimentary period (~42 Ma), the Pacific Plate subduction direction changed significantly from NW to NWW, generating a right-lateral stress field in the Bohai Bay Basin. Here, the pre-existing Tan-Lu fault zone acted as a key right-lateral strike-slip fault zone. Under simple shear stress, Riedel shear fractures formed (Lu et al., 2018b; Soumaya et al., 2020; Yuan et al., 2024), such as WJG (Yuan et al., 2022), alongside numerous normal strike-slip faults (θ=35°-45°). NNE-SSW normal strike-slip faults were developed with low growth rates, exhibiting displacements typically within 0.30 - 0.55 km during this period. (b) Region B, located between the Tan-Lu and Lan-Liao fault zones but away from them (Fig. 13), exhibited significant variability in the strike of the 4 master faults (110° - 200°), while the strike of the branch faults remained relatively constant (140° - 150°). Here, the simple shear effect weakened while pure shear became dominant (Yuan et al., 2022; Chu et al., 2024), manifesting as NW-SE extension. Faults primarily exhibited normal faulting characteristics; meanwhile, faults with other orientations, particularly NE-striking ones, displayed dextral strike-slip motion. The overall activity was therefore dominated by extension with a subordinate strike-slip component, leading to the prevalence of strike-slip normal faults (θ=45°-80°). This occurred due to buffering from the distant boundary faults, with extension primarily controlled by asthenospheric upwelling beneath the central depression. (c) Region C experienced the combined effects of early right-lateral strike-slip action from deep faults, such as the Lan-Liao fault zone (Fig. 13), and late NNW extensional action. Normal strike-slip faults (θ=40°-45°) formed due to transmitted right-lateral shear from

the Lan-Liao fault zone, though, unlike in Region A, this effect was weakened by greater distance from the Pacific subduction front. This combination resulted in significant strike-slip and extensional displacement components (Wu et al., 2012), leading to the evolution of normal strike-slip faults.

5.3. Error analysis between the quantitative calculation and stereographic projection methods

Adopting eleven primary fault zones in the JYD as case studies, the error between the results of true pitch angle (θ) obtained by the two methods is mostly less than 5% (Table 3, 4). This does not significantly affect the final interpretation of the fault kinematic properties (unless the calculation happens to straddle both criteria). This indicates the efficacy of the pitch angle calculation in characterizing the kinematic attributes of fault zones.

As for the error between the two methods, there are four possible factors. (a) Error in rock mass inelastic deformation. This study neglects the influence of complex plastic deformation, modelling fault-blocks as undergoing rigid bodies motion in a brittle deformation state. This assumption ensures that the displacement of piercing point pairs represents the entire fault-block's motion, significantly simplifying the problem while introducing a notable source of error However, minor displacements of branch faults and fault-block movements within the depression scale (e.g., Fig. 9 b, c, d) demonstrate

rigid-body characteristics. Thus, the rigid-body approximation remains adequate for this study. (b) Error in the acquisition of original data. The data used by the two methods are not the same, and considering that the shape of the actual fault is not changed, reading the relevant data and applying it in the theoretical model may lead to mismatches after the conversion of parameters. (c) The results obtained by the two methods are different on time scales. Theoretically, the quantitative calculation method of geometry based on parameters such as the strike-slip component of a tectonic zone reflects the cumulative effects from the sediment deposition until the present, whereas the stereographic projection method is the analysis of the state of a specific horizon. (d) The contribution of each branch fault to the deformation of the fault zone is different. The stereographic projection method is a direct average calculation of the local analytic results of each branch fault. When there is a branch fault with a small displacement and its dip and dip angle are very different from other branch faults, even if it does not contribute much to the deformation, it is still weighted equally in the final calculation. Notably, the calculated results of F_8 at the bottom of E_3s_1 have a larger error (8.96%, Table 4), then we can see from the stereographic projection (Fig. 12q) that the intersection points of branch faults and master faults are distributed over a large range, and the average value of analytical results cannot accurately reflect their actual contribution to deformation. To mitigate such errors, the solutions will focus on: (1) utilizing higher-precision geological and seismic data; (2) targeting identification of minor-displacement branch faults; and (3) developing weight-balancing approaches for

displacement contributions of individual branch faults based on geological significance.

5.4. Innovativeness of the new model

The novel model for analysis of kinematic properties of faults presented here is based on the principle of dividing the development of branch faults into two cases, which are located at the tip and the lateral part of the master fault, so as to adapt to the actual development characteristics of different fault zones. There are two main advantages of this model; these are considered next.

In one respect, this model reduces the difficulty of relying solely on the identification of piercing points from physical geological bodies or those imaged in seismic data, and expands the opportunity for application of this analytical approach. Previous analyses relied heavily on finding faulted gravel layers, river channels, etc., as piercing points to calculate the strike-slip displacement components of fault zones. This model simplifies the characteristics of a fault zone. The intersection points of the master fault and each branch fault on the footwall and hanging wall on the same horizon are widely defined as the piercing points, which greatly expands the application of this quantitative calculation method. In other words, this model can be applied to almost all fault zones except for en echelon fault zones that lack a master fault.

In a second respect, the local and global developmental characteristics of fault zones

can be compared by this model. When employing the aforementioned methods to analyze the kinematic properties of fault zones in the JYD, it was found that the fault zone was not only heterogeneous in the $E_2s_3^L$ sedimentary period (Yao et al. 2023), but also demonstrates inconsistent properties of activity of the fault slip lines of the branch faults located on the same side of a master fault (Fig. 12q). It is shown that the fault zone has the heterogeneity of segmental activity and local kinematics in space and time (Han et al., 2017). For instance, F_{11}, namely the Linshang fault zone, contains the master fault (F), with a horsetail structure in the north (F_1-F_4 in Fig. 8b). According to the true pitch angle (44.20°) calculated by Eq. (3), (4), (7) and (8). F_{11} is identified as an R-type right-lateral strike-slip fault zone (44.20°). Meanwhile, the stereographic projection method yielded a result suggesting a normal strike-slip fault (40.29°). However, on a smaller scale, the pitch angle of sharp intersection angles between F and branch faults calculated by Eq. (6) range from 42° to 47°, the kinematic properties of one of the branch faults F_2 indicated a strike-slip normal fault with θ>45°. Quantitative geometric analysis of F_{11} shows that the middle section of the master fault (F) has a larger dip slip component than the branch faults, but for F itself, the cumulative dip slip distances at both ends exceed the corresponding data in the middle. In general, F_{11} is dominated by NE-SW strike-slip faults, which also develop EW-, NS- and NEE-striking branching faults and regulating faults, suggesting a multi-phase activity history for this tectonic pattern (Liu et al., 2018; Hu et al., 2019). These faults have a complex tectonic origin, some of which are derived from strike-slip activities, while others are related faults

formed due to the difference of displacement during extension.

5.5. Analysis of the two methods combined in the new model

Both methods can effectively identify the kinematic properties of fault zones quantitatively, including those of local branch faults. Combined with error analysis, the quantitative calculation method of fault geometry requires calculation of a comprehensive θ value after summing the displacement components of each branch fault, which may provide a more accurate result, but requires higher quality data. These precise geological and seismic datasets help identify all branch faults as comprehensively as possible and accurately reflect their geometric relationships with the master fault, thereby improving the accuracy of the calculation method. Conversely, lower-resolution data may miss minor faults that contribute to fault activity, leading to potential errors. For example, 3D seismometers or other data are needed to confirm the displacement of all faults. Therefore, when the data in the study area is insufficient to enable implementation of the specific and accurate calculation method, the projection method may still be applied as a valuable and worthwhile alternative method for quantitative analysis. In addition, the projection method can also be used to analyze the kinematic characteristics of local branch faults. The most notable advantage of the projection method is that it derives results directly through projection on a Wulff net, requiring fewer specific data and avoiding complex statistical and computational steps. A current limitation of this method is that when multiple branch faults are present, the

results for each are independently derived, and the reliability of the outcome depends on the rationale for selecting representative faults. In this regard, comparing averaged, weighted-averaged, or median values of the pitch angle with results from geometric calculations—while considering practical geological significance—could be a direction for future improvement.

6. Conclusions

(1) A new fault zone model is proposed to greatly reduce the difficulty of identifying piercing points and calculating the strike-slip displacement of components. This new model significantly expands the application of kinematic analysis based on the fault slip lines of fault zones. Moreover, the kinematic properties of any point on the master fault can be calculated to conduct localized or overall research on the fault zone, making the theoretical model highly adaptable.

(2) The quantitative calculation method of fault geometry requires identifying the fault slip line between intersecting faults and calculating displacement components and key kinematic parameters of a fault zone through the geometric relationship in mathematics, such as the true pitch angle (θ). Although this method yields precise results, its accurate implementation requires high-quality data

(3) A new application of the stereographic projection method is introduced for the

quantitative analysis of fault kinematic properties. It uses the Wulff net and the principle of stereoscopic projection to analyze the values of related parameters from the perspective of geology. This approach can avoid extensive statistical and computational work; however, in cases with multiple branch faults, the accuracy of the results depends on the rationale for selecting representative branch faults.

(4) The application of the model in the Jiyang Depression yielded satisfactory results. Through the analysis of quantitative calculation results, the evolution of fault zones of the Jiyang Depression during the $E_2s_3^L$ period (about 42.0 – 38.0 Ma) reveal different characteristics, but was overall dominated by right-lateral strike-slip. Extension-strike-slip areas developed in the eastern and western parts of the depression, influenced by the adjacent pre-existing Tan-Lu and Lan-Liao fault zones, respectively. The middle part is an area of overlap between pre-existing fault zones, which was dominated by extensional action. This structural pattern resulted from a right-lateral stress field generated by a significant change in the Pacific Plate subduction direction.

Acknowledgements

The Sinopec Shengli Oilfield (SLOF) kindly supplied the basic geological, 2D, and 3D seismic data. This study was supported by the National Natural Science Foundation of China Program "Strike-slip structure and hydrocarbon relationship of the Cenozoic in Jiyang Depression" (No. 42172138) and research program of SLOF namely

"Quantitative characterization of different types of strike-slip faults in the Cenozoic in Jiyang Depression" (No. 30200018-19-ZC0613-0118). The authors thank editor-in chief and anonymous reviewers for their valuable comments and advice that have improved this manuscript. We also thank MJEditor (www.mjeditor.com) for provision of English language editing services during the preparation of this manuscript.

CRediT authorship contribution statement

Qiwei Gou: Conceptualization, Methodology, Software, Investigation, Formal analysis, Writing – original draft, Writing - review & editing. **Shuping Chen**: Visualization, Writing - review & editing, Supervision, Project administration, Funding acquisition. **Yifan Du**: Investigation, Writing - review & editing. **Adam D. McArthur**: Writing – review & editing, Supervision. **Nigel P. Mountney**: Writing – review & editing, Supervision. **Haowei Yuan**: Visualization, Software. **Xi Li**: Investigation. **Huaibo Zhao**: Investigation.

References

Benesh, N.P., Plesch, A., Shaw, J. H., 2014. Geometry, kinematics, and displacement characteristics of tear-fault systems: An example from the deep-water Niger Delta. AAPG Bull. 98(3), 465-482. https://doi.org/10.1306/06251311013.

Biddle, K. T., Christie-Blick, N., 1985. Strike-slip deformation, basin formation, and sedimentation. SEPM Society for Sedimentary Geology.

Chen, S., Liu, X., Cui, Y., Zhao, X., Zhang, J., 2017. Palaeogene structural evolution of Dongying Depression, Bohai Bay Basin, NE China. Int. Geol. Rev. 59(3), 259-273. https://doi.org/10.1080/00206814.2016.1223559.

Chen, S.P., Liu, J.Y., Gou, Q.W., Yuan, H.W., 2022. Mechanical mechanisms and deformation characteristics of strike-slip structures in sedimentary basins. Geol. Rev. 68(5): 1729-1742. https://doi.org/10.16509/j.georeview.2022.04.041 (in Chinese with English abstract).

Chen, S.P., Tian, Z.J., Xu, S.D., Ma, Z.Z., Chang, S.Y., Zhao, H.B., 2024. Two structural types of shear fracture belts related to wrenches. Geology Bulletin of China 43(1):13-19. 10.12097/gbc.2023.04.005.

Cheng, Y.J., Wu, Z.P., Lu, S.N., Li, X., Lin, C.Y., Huang, Z., Huang, Z., Su, W., Jiang, C., Wang, S.Y., 2018. Mesozoic to Cenozoic tectonic transition process in Zhanhua Sag, Bohai Bay Basin, east China. Tectonophysics 730, 11-28. https://doi.org/10.1016/j.tecto.2018.02.010.

Chu, R., Yan, D. P., Qiu, L., Chang, D. S., Wang, Q., Song, X. Q., Wang, C., 2024. Strain partitioning dominated growth of strike-slip fault: Insight from the Tan-Lu fault in Eastern China. J. Struct. Geol. 182, 105126. https://doi.org/10.1016/j.jsg.2024.105126.

Dimmen, V., Rotevatn, A., Peacock, D. C., Nixon, C. W., Nærland, K. 2017. Quantifying structural controls on fluid flow: Insights from carbonate-hosted fault damage zones on the Maltese Islands. J. Struct. Geol. 101, 43-57.

https://doi.org/10.1016/j.jsg.2017.05.012.

Dooley, T., McClay, K., Bonora, M., 1999. 4D evolution of segmented strike-slip fault systems: applications to NW Europe// Geological Society, London, Petroleum Geology Conference Series. Geo. Soc. London Special Pub. 5(1): 215-225. https://doi.org/10.1144/0050215.

Dooley, T., Schreurs, G., 2012. Analogue modelling of intraplate strike-slip tectonics: A review and new experimental results. Tectonophysics 574, 1-71. https://doi.org/10.1016/j.tecto.2012.05.030.

Fedorik, J., Zwaan, F., Schreurs, G., Toscani, G., Bonini, L., Seno, S., 2019. The interaction between strike-slip dominated fault zones and thrust belt structures: Insights from 4D analogue models. J. Struct. Geol. 122, 89-105. https://doi.org/10.1016/j.jsg.2019.02.010.

Ferrill, D. A., Smart, K. J., Cawood, A. J., Morris, A. P., 2021. The fold-thrust belt stress cycle: Superposition of normal, strike-slip, and thrust faulting deformation regimes. J. Struct. Geol. 148, 104362. https://doi.org/10.1016/j.jsg.2021.104362.

Fletcher, J.M., Teran, O.J., Rockwell, T.K., Oskin, M.E., Hudnut, K. W., Spelz, R.M., Lacan, P., Dorsey, M.T., Ostermeijer, G., Mitchell, T.M., Akciz, S.O., Hernandez-Flores, A.P., Hinojosa-Corona, A., Peña-Villa, I., Lynch, D.K., 2020. An analysis of the factors that control fault zone architecture and the importance of fault orientation relative to regional stress. GSA Bull. 132(9-10): 2084-2104. https://doi.org/10.1130/B35308.1.

Fossen, H., 2016. Structural Geology (2nd ed.). Cambridge University Press. Page 287.

Fossen, H., Rotevatn, A., 2016. Fault linkage and relay structures in extensional settings-A review. Earth Sci. Rev. 154: 14-28. https://doi.org/10.1016/j.earscirev.2015.11.014.

Fu, S.T., Ma, D.D., Guo, Z.J., Cheng, F., 2015. Strike-slip superimposed Qaidam Basin and its control on oil and gas accumulation, NW China. Petrol. Explor. Dev+. 42(6), 778-789. https://doi.org/10.1016/S1876-3804(15)30074-4.

Garfunkel, Z., Ron, H. 1985. Block rotation and deformation by strike‐slip faults: 2. The properties of a type of macroscopic discontinuous deformation. J. Geophys. Res. Solid Earth. 90. (B10), 8589-8602.

Gogonenkov, G.N., Timurziev, A.I., 2012. Strike-slip faulting in the West Siberian Platform: Insights from 3D seismic imagery. C. R. Geosci. 344(3-4): 214-226. https://doi.org/10.1016/j.crte.2011.09.010.

Gou, Q.W., Jiang, Y.L., Liu, J.D., Lv, X.Y., Jiang, Y.W., 2020. Hydrocarbon accumulation conditions and patterns of the Mesozoic and Paleozoic in Wangguantun area of Huanghua Depression. PGRE. 27(6): 57-64. https://doi.org/10.13673/j.cnki.cn37-1359/te.2020.06.007 (in Chinese with English abstract).

Han, X.Y., Deng, S, Tang, L.J., Cao, Z.C., 2017. Geometry, kinematics and displacement characteristics of strike-slip faults in the northern slope of Tazhong uplift in Tarim Basin: A study based on 3D seismic data. Mar. Petrol. Geol. 88: 410-427. https://doi.org/10.1016/j.marpetgeo.2017.08.033.

Harding, T.P., 1974. Petroleum traps associated with Wrench faults. AAPG Bull. 58(7): 1290-1304.

Howarth, R.J. 1996. History of the stereographic projection and its early use in geology. Terra Nova 8(6), 499-513.

Hu, P., Yang, F., Zhang, R., Wang, W., Dong, R., 2022. Cenozoic extension to strike-slip transition in the Liaodong Bay Subbasin along the Tan-Lu Fault Zone, Bohai Bay Basin: new insights from stress field modelling. Tectonophysics 822, 229163.

Hu, Z.W., Xu, C.G., Wang, D.Y., Ren, J., Liu, Y.B., Xiao, S.G., Zhou, X., 2019. Superimposed characteristics and genetic mechanism of strike-slip faults in the Bohai Sea, China. Petrol. Explor. Dev+. 46(2), 265-279. https://doi.org/10.1016/S1876-3804(19)60007-8.

Hughes, A., 2012. Book Review: Structural Geology: By Haakon Fossen, Cambridge University Press, 2010, ISBN: 978-0-521-51664-8 (hardback), USD 70.00. Pure Appl. Geophys. 169, 289-292.

Jia, C.Z., Ma, D.D., Yuan, J.Y., Wei, G.Q., Yang, M., Yan, L., Tian, F.L., Jiang, L. 2022. Structural characteristics, formation & evolution and genetic mechanisms of strizke-slip faults in the Tarim Basin. Natural Gas Industry B 9(1), 51-62. https://doi.org/10.1016/j.ngib.2021.08.017.

Jolly, B. A., Lonergan, L., Whittaker, A. C., 2016. Growth history of fault-related folds and interaction with seabed channels in the toe-thrust region of the deep-water Niger delta. Mar. Petrol. Geol. 70, 58-76. https://doi.org/10.1016/j.marpetgeo.2015.11.003.

Koons, P. O., Norris, R. J., Craw, D., Cooper, A. F., 2003. Influence of exhumation on the structural evolution of transpressional plate boundaries: An example from the Southern Alps, New Zealand. Geology 31(1), 3-6. https://doi.org/10.1130/0091-7613(2003)031<0003:IOEOTS>2.0.CO;2.

Le Guerroué, E., Cobbold, P.R., 2006. Influence of erosion and sedimentation on strike-slip fault systems: insights from analogue models. J. Struct. Geol. 28(3): 421-430. https://doi.org/10.1016/j.jsg.2005.11.007.

Li, W., Meng, M.F., Chen, X.P., Zhang, T.J., Niu, C.M., Wu, Z.P., Feng, J.W., 2021. Quantitative characterization of derivative extension and extrusion of curved strike-slip fault in eastern Bohai Sea and its petroleum geological significance. J. China Uni. Petrol. (Natural Sci.). 45(5):23-32. https://doi.org/10.3969/j.issn.1673-5005.2021.05.003.

Li, Z.T., Liu, B.R., Liu, Y.,J. Yuan, J.L., Zhou, Q.J., Li, S.Z., Guan, Q.B., Wang, G.Z., 2024. Mesozoic to Cenozoic tectonic evolution in the central Bohai Bay Basin, East China. GSA Bulletin, 136(11-12), 4965-4984. https://doi.org/10.1130/B37427.1.

Liang, J.T., Wang, H.L., Bai, Y., Ji, X.Y., Duo, X.M., 2016. Cenozoic tectonic evolution of the Bohai Bay Basin and its coupling relationship with Pacific Plate subduction. J. Asian Earth Sci. 127, 257-266. https://doi.org/10.1016/j.jseaes.2016.06.012.

Lindsay, M.D., Aillères, L., Jessell, M.W., de Kemp, E.A., Betts, P. G., 2012. Locating and quantifying geological uncertainty in three-dimensional models: Analysis of the Gippsland Basin, southeastern Australia. Tectonophysics 546, 10-27. https://doi.org/10.1016/j.tecto.2012.04.007.

Liu, H.F., 1993. Dynamic classification of sedimentary basins and their structural styles. Earth Sci. 6:699-724+814 (in Chinese with English abstract).

Liu, Q.Y., He, L.J., Chen, LC., 2018. Tectono-thermal modeling of Cenozoic multiple rift episodes in the Bohai Bay Basin, eastern China and its geodynamic implications. IINT J EARTH SCI, 107(1), 53-69. https://doi.org/10.1007/s00531-017-1550-1.

Liu, R., Li, A., Zhang, S.M., Guo, C.H., Chen, Z.D., 2020. A NW-striking dextral strike-slip fault at the eastern end of the Altyn Tagh fault and its tectonic implications for northeastward growth of the Tibetan Plateau. J. Asian Earth Sci. 188:104069. https://doi.org/10.1016/j.jseaes.2019.104069.

Lu, S.K., Wang, S.J., Liu, H.J., Jia, X.M., Wang, D., 2018a. A quantitative method to determine fault slip parameters with 3D seismic data. Acta Geol. Sin. 39(3):304-313. https://doi.org/10.7623/syxb201803005.

Lu, S.N., Wu, Z.P., Cheng, Y.J., Li, X., 2018b. Division of differential tectonic evolution in Shengli shallow sea area of Jiyang Depression. PGRE. 25(4):61-66. https://doi.org/10.13673/j.cnki.cn37-1359/te.2018.04.010 (in Chinese with English abstract).

Ma, B.S., Liang, H., Wu G.H., Tang, Q.S., Tian, W.Z., Zhang, C., Yang, S., Zhong, Y., Zhang, X., Zhang, Z.L., 2023. Formation and evolution of the strike-slip faults in the central Sichuan Basin, SW China. Petrol. Explor. Dev+. 50(2), 373-387. https://doi.org/10.1016/S1876-3804(23)60394-5.

Ma, D.B., Wang, Z.C., Duan, Shufu, Gao, J.R., Jiang, Q.C., Jiang, H., Zeng, F.Y., Lu,

W.H., 2018. Strike-slip faults and their significance for hydrocarbon accumulation in Gaoshiti-Moxi area, Sichuan Basin, SW China. Petrol. Explor. Dev+. 45 (5): 795-805. https://doi.org/10.1016/S1876-3804(18)30088-0.

Mansinha, L.A., Smylie, D.E., 1971. The displacement fields of inclined faults. B. Seismol. Soc. AM. 61(5): 1433-1440. https://doi.org/10.1785/BSSA0610051433.

Marrett, R., Allmendinger, R.W., 1990. Kinematic analysis of fault-slip data. J. Struct. Geol. 12(8): 973-986. https://doi.org/10.1016/0191-8141(90)90093-E.

Molnar, P., Tapponnier, P., 1977. Relation of the tectonics of eastern China to the India-Eurasia collision: Application of slip-line field theory to large-scale continental tectonics. Geology 5(4): 212-216. https://doi.org/10.1130/0091-7613(1977)5<212:ROTTOE>2.0.CO;2.

Morley, C.K., 2007. Variations in Late Cenozoic–Recent strike-slip and oblique-extensional geometries, within Indochina: The influence of pre-existing fabrics. J. Struct. Geol. 29(1): 36-58. https://doi.org/10.1016/j.jsg.2006.07.003.

Mouslopoulou, V., Nicol, A., Little, T.A., Walsh, J.J., 2007. Displacement transfer between intersecting regional strike-slip and extensional fault systems. J. Struct. Geol. 29(1): 100-116. https://doi.org/10.1016/j.jsg.2006.08.002.

Peacock, D.C.P., 1991. Displacements and segment linkage in strike-slip fault zones. J. Struct. Geol. 13(9): 1025-1035. https://doi.org/10.1016/0191-8141(91)90054-M.

Sançar, T., Zabcı, C., Akcar, N., Karabacak, V., Yeşilyurt, S., Yazıcı, M., Akyüz, H.S., Önal, A.Ö., Ivy-Ochs, S., Christl, M., Vockenhuber, C., 2020. Geodynamic importance

of the strike-slip faults at the eastern part of the Anatolian Scholle: Inferences from the uplift and slip rate of the Malatya Fault (Malatya-Ovacık Fault Zone, eastern Turkey). J. Asian Earth Sci. 188: 104091. https://doi.org/10.1016/j.jseaes.2019.104091.

Riedel, W., 1929. Zur mechanik geologischer brucherscheinungen. Zentral-blatt fur Mineralogie. Geologie und Paleontologie B. 354-368.

Shaanan, U., Rosenbaum, G., Li, P., Vasconcelos, P., 2014. Structural evolution of the early Permian Nambucca Block (New England Orogen, eastern Australia) and implications for oroclinal bending. Tectonics 33(7), 1425-1443. https://doi.org/10.1002/2013TC003426.

Song, M., 2018. The exploration status and outlook of Jiyang Depression. China Petrol. Explor. 23(3): 11. https://doi.org/10.3969/j.issn.1672-7703.2018.03.002 (in Chinese with English abstract).

Soumaya, A., Kadri, A., Ayed, N. B., Kim, Y. S., Dooley, T. P., Rajabi, M., Braham, A., 2020. Deformation styles related to intraplate strike-slip fault systems of the Saharan-Tunisian Southern Atlas (North Africa): New kinematic models. J. Struct. Geol. 140, 104175. https://doi.org/10.1016/j.jsg.2020.104175.

Stefanov, Y. P., Bakeev, R. A., 2014. Deformation and fracture structures in strike-slip faulting. Engineering Fracture Mechanics, 129, 102-111. https://doi.org/10.1016/j.engfracmech.2014.05.019.

Tapponnier, P., Molnar, P., 1976. Slip-line field theory and large-scale continental tectonics. Nature 264(5584): 319-324. https://doi.org/10.1038/264319a0.

Teng, C.Y., Xu, C.G., Niu, C.M., Guan, D.Y., Zou, H.Y., Hao, F., 2019. Tectonic evolution of the Penglai 7–6 structure and its implications for petroleum exploration in a releasing bend of a strike-slip fault system, Tan-Lu fault zone, east China. Mar. Petrol. Geol. 109, 658–674. https://doi.org/10.1016/j.marpetgeo.2019.06.052.

Waldron, J.W.F., Barr, S.M., Park, A.F., White, C.E., Hibbard. J., 2015. Late Paleozoic strike-slip faults in Maritime Canada and their role in the reconfiguration of the northern Appalachian orogen. Tectonics 34(8): 1661-1684. https://doi.org/10.1002/2015TC003882.

Walker, R.T., Bezmenov, Y., Begenjev, G., Carolin, S., Dodds, N., Gruetzner, C., Jackson, J.A., Mirzin, R., Mousavi, Z., Rhodes. E.J., 2021. Slip-rate on the Main Köpetdag (Kopeh Dagh) strike-slip fault, Turkmenistan, and the active tectonics of the South Caspian. Tectonics 40(8): e2021TC006846. https://doi.org/10.1029/2021TC006846.

Williams, G., Vann, I., 1987. The geometry of listric normal faults and deformation in their hangingwalls. J. Struct. Geol. 9(7): 789-795. https://doi.org/10.1016/0191-8141(87)90080-0.

Woodcock, N.H., Rickards, B., 2003. Transpressive duplex and flower structure: Dent fault system, NW England. J. Struct. Geol. 25(12): 1981-1992. https://doi.org/10.1016/S0191-8141(03)00057-9.

Wu, K.Y., Zhao, Z.X., Cui, S.L., Li, J.Y., 2012. Controlling of Xiakou fault on hydrocarbon accumulation in the southern part of Huimin Depression. Int. J. Geomech.

18(1):32-41 (in Chinese with English abstract).

Xu, W., Qiu, N.S., Li, Y., 2019. Evolution of the Cenozoic thermal lithosphere of the Jiyang Sub-basin, Bohai Bay Basin: Implications for the lithospheric thinning mechanism. Tectonics 773, 228229. https://doi.org/10.1016/j.tecto.2019.228229.

Yao, Y., Zeng, L., Mao, Z., Han, J., Cao, D., Lin, B., 2023. Differential deformation of a strike-slip fault in the Paleozoic carbonate reservoirs of the Tarim Basin, China. J. Struct. Geol. 173, 104908. https://doi.org/10.1016/j.jsg.2023.104908.

Yu, J., Walker, R.T., Rhodes, E.J., Zhang, P., Li, C., Wang, S., Wang, Y., Liu, F., Hao. Y., 2021. East Tacheng (Qoqek) fault zone: Late quaternary tectonics and slip rate of a left‐lateral strike‐slip fault zone north of the Tian Shan. Tectonics 40(2): e2020TC006377. https://doi.org/10.1029/2020TC006377.

Yu, Y., Zhou, X., Xu, C., Wu, K., Lv, D., Liu, Y., Zhou, X., 2020. Architecture and evolution of the Cenozoic offshore Bohai Bay basin, eastern China. J. Asian Earth Sci. 192, 104272. https://doi.org/10.1016/j.jseaes.2020.104272.

Yu, Z.H., Han, Q., Dong, D.D., 2008. Estimation of Cenozoic dextral strike-slip displacement of Tan-Lu fault in Laizhou Bay. Natural Gas Geosci. 1:62-69 (in Chinese with English abstract).

Yuan, H.W., Chen, S.P., Dai, K., Jia, G.H., Wang, P.F., Li, J.Y., Gou, Q.W., 2022. Cenozoic tectonic evolution of the Bohai Bay Basin: Constraints from strike-slip activities of the Wangjiagang fault zone, NE China. J. Asian Earth Sci. 2022, 233: 105262. https://doi.org/10.1016/ j.jseaes.2022.105262.

Yuan, H.W., Dai, K., Zhang, C., Liu, L.B., Jing, T.Y., Li, J.Y., Zhao, W.T., Chen, F., 2024. Cenozoic sedimentary archives of a strike-slip fault zone in the Tanhai Region, Bohai Bay Basin, Northeastern China. J. Struct. Geol. 186, 105203. https://doi.org/10.1016/j.jsg.2024.105203.

Zhang, L.Y., Bao, Y.S., Li, J.Y., Li, Z., Zhu, R.F., Zhang, J.G., 2014. Movability of lacustrine shale oil: a case study of Dongying Sag, Jiyang Depression, Bohai Bay Basin. Petrol. Explor. Dev+. 41(6), 703-711. https://doi.org/10.1016/S1876-3804(14)60084-7.

Zhang, W.Z., Zha, M., Zhang, Y.Y., 2017. Cenozoic transtensional structural styles and their controls over hydrocarbon accumulation in Dongying Depression. Oil & Gas Geol. 38(6):1052-1058.

Zhao, L., Li, L., Zhang, H., 2014. Fault systemls kinematic characteristics and dynamic mechanism during early Cenozoic in Dongying Sag. J. China Uni. Petrol. (Natural Sci.). 38(3):18-24.

Zhou, X.H., Zhang, X.T., Niu, C.M., 2019. Growth of strike-slip zone in the southern Bohai Bay Basin and its significances for hydrocarbon accumulation. Oil & Gas Geol. 40(2):215–222.

Zhu, Y.B., Liu, S.F., Zhang, B., Gurnis, M., Ma, P.F., 2021. Reconstruction of the Cenozoic deformation of the Bohai Bay basin, North China. BASIN RES, 33(1), 364-381. https://doi.org/10.1111/bre.12470.

Zielke, O., Klinger, Y., Arrowsmith, J.R., 2015. Fault slip and earthquake recurrence along strike-slip faults—Contributions of high-resolution geomorphic data.

Tectonophysics 638: 43-62.

Zoback, M. D., Stephenson, R. A., Cloetingh, S., Larsen, B. T., Van Hoorn, B., Robinson, A., Horvath, F., Puigdefabregas, C., Ben-Avraham, Z., 1993. Stresses in the lithosphere and sedimentary basin formation. Tectonophysics 226(1-4), 1-13. https://doi.org/10.1016/0040-1951(93)90107-U.

Zuo, Y.H., Qiu, N.S., Li, J.W., Hao, Q.Q., Pang, W.Q., Zhao, Z.Y., Zhu, Q., 2015. Meso-cenozoic tectono-thermal evolution history in Bohai Bay Basin, North China. J. Earth Sci. 26, 352-360. https://doi.org/10.1007/s12583-014-0500-0.

Appendices: Equations

$$D_d = l_{M'N} \cdot \sin\lambda \quad \text{Eq. (1)}$$

$$D_s = l_{M'N} \cdot \cos\lambda \quad \text{Eq. (2)}$$

$$\lambda = \arctan\frac{D_d}{D_s} \quad \text{Eq. (3)}$$

$$\theta = \arctan\frac{D_q}{D_s} = \arctan\frac{\tan\lambda}{\cos\alpha} = \arctan\frac{D_d}{\cos\alpha \cdot D_s} \quad \text{Eq. (4)}$$

$$\tan\theta = \frac{D_q}{D_s} < 1 \quad \text{Eq. (5)}$$

$$\lambda_i = \arctan\frac{D_{di}}{D_{si}} \quad \text{Eq. (6)}$$

$$D_d = \sum_1^n D_{di} = \sum_1^n l_{Mi'Ni} \cdot \sin\lambda_i \quad \text{Eq. (7)}$$

$$D_s = \sum_1^n D_{si} = \sum_1^n l_{Mi'Ni} \cdot \cos\lambda_i \quad \text{Eq. (8)}$$

$$\alpha = \text{acrtan}\frac{l_v}{l_h} \quad \text{Eq. (9)}$$

$$\cos\theta = \cos\lambda \cdot \cos\gamma \quad \text{Eq. (10)}$$

$$\sin\theta = \frac{\sin\gamma}{\sin\alpha} \qquad \text{Eq. (11)}$$

The detailed derivation processes of key equations (4), (10) and (11):

(a) The derivation process of Eq. (4) is as follows:

After obtaining the dip (α), strike-slip (D_s) and dip-slip (D_d) displacement components of the master fault, the true pitch angle (θ) can be obtained from Eq. (4).

As can be easily seen from Fig. 5,

$$D_q = \frac{D_d}{\cos\alpha}$$
$$D_d = \frac{D_d}{\tan\lambda}$$

Therefore,

$$\theta = \arctan\frac{D_q}{D_s} = \arctan\frac{\tan\lambda}{\cos\alpha} \qquad \text{Eq. (4.1)}$$

Furthermore, by combining Eq. (3), the latter part of Eq. (4) can be obtained:

$$\theta = \arctan\frac{\tan\lambda}{\cos\alpha} = \arctan\frac{D_d}{\cos\alpha \cdot D_s} \qquad \text{Eq. (4.2)}$$

(b) The derivation process of Eq. (10) is as follows:

As can be easily seen from Fig. 5,

$$l_{MN} = \frac{l_{M'N}}{\cos\gamma}$$

Therefore, by combining Eq. (2), Eq. (10) can be obtained:

$$\cos\theta = \frac{D_s}{l_{MN}} = cos\lambda \cdot cos\gamma \qquad \text{Eq. (10)}$$

(c) The derivation process of Eq. (11) is as follows:

As can be easily seen from Fig. 5,

$$D_q = \frac{l_v}{\sin\alpha}$$

$$l_{MN} = \frac{l_v}{\sin\gamma}$$

Therefore, Eq. (11) can be obtained:

$$\sin\theta = \frac{D_q}{l_{MN}} = \frac{\sin\gamma}{\sin\alpha} \qquad \text{Eq. (11)}$$